

1 Single-cell transcriptional profiling of clear cell renal cell carcinoma reveals an invasive tumor  
2 vasculature phenotype

3

4 Justina Zvirblyte<sup>1</sup>, Juozas Nainys<sup>1,§</sup>, Simona Juzenas<sup>1</sup>, Raimonda Kubiliute<sup>2</sup>, Marius  
5 Kincius<sup>3</sup>, Albertas Ulys<sup>3</sup>, Sonata Jarmalaite<sup>2,3,\*</sup> and Linas Mazutis<sup>1,\*</sup>

6

7 <sup>1</sup>Institute of Biotechnology, Life Sciences Center, Vilnius University, Vilnius, 10257, Lithuania

8 <sup>2</sup> Institute of Biosciences, Life Sciences Center, Vilnius University, Vilnius, 10257, Lithuania

9 <sup>3</sup> National Cancer Institute, Vilnius, 08660, Lithuania

10 <sup>§</sup> Current address: Atrandi Biosciences, Vilnius, 10257, Lithuania,

11

12 Keywords: renal cancer, tumor vasculature, tumor endothelial cells, tip cells, single cell RNA  
13 sequencing

14

15

16 \* Corresponding author: [linas.mazutis@btu.vu.lt](mailto:linas.mazutis@btu.vu.lt)

17 \* Co-corresponding author: [sonata.jarmalaite@nvi.lt](mailto:sonata.jarmalaite@nvi.lt)

18

19

20

21

22

23 **ABSTRACT**

24

25 Clear cell renal cell carcinoma (ccRCC) is the most prevalent form of renal cancer,  
26 accounting for over 75% of cases. The asymptomatic nature of the disease contributes to late-  
27 stage diagnoses and poor survival. Highly vascularized and immune infiltrated  
28 microenvironment are prominent features of ccRCC, yet the interplay between vasculature  
29 and immune cells, disease progression and response to therapy remains poorly understood.  
30 Using droplet-based single-cell RNA sequencing we profiled 50,236 transcriptomes from  
31 paired tumor and healthy adjacent kidney tissues. Our analysis revealed significant  
32 heterogeneity and inter-patient variability of the tumor microenvironment. Notably, we  
33 discovered a previously uncharacterized vasculature subpopulation associated with epithelial-  
34 mesenchymal transition. The cell-cell communication analysis revealed multiple modes of  
35 immunosuppressive interactions within the tumor microenvironment, including clinically  
36 relevant interactions between tumor vasculature and stromal cells with immune cells. The  
37 upregulation of the genes involved in these interactions was associated with worse survival in  
38 the TCGA KIRC cohort. Our findings demonstrate the role of tumor vasculature and stromal  
39 cell populations in shaping the ccRCC microenvironment and uncover a subpopulation of cells  
40 within the tumor vasculature that is associated with an invasive phenotype.

41 **INTRODUCTION**

42

43 The asymptomatic nature of clear cell renal cell carcinoma (ccRCC), the most common  
44 renal cancer, often leads to diagnosis in late III or IV stage with survival probability of 59% and  
45 20%, respectively. Approximately 30% of cases metastasize<sup>1</sup>. Previous efforts aimed at  
46 characterizing ccRCC tumors have provided valuable insights into the genomic<sup>2</sup>,  
47 transcriptomic and epigenetic<sup>3,4</sup> landscape of both the tumor and the tumor microenvironment  
48 (TME). It is now well-established that the most abundant genomic alterations in ccRCC involve  
49 the loss of regions in 3p chromosome (occurring in >90% of cases) and von Hippel–Lindau  
50 (VHL) gene mutations (>50% of cases). These alterations lead to impaired degradation and  
51 abnormal accumulation of hypoxia-inducible factors (HIFs)<sup>2,3</sup>, resulting in a highly vascularized  
52 tumor appearance. Moreover, ccRCC tumors exhibit a high degree of immune infiltration<sup>5,6</sup>.  
53 Consequently, the most common first-line treatment options for the localized disease involve  
54 surgical removal of the tumor, while advanced disease may be treated with VEGF pathway  
55 inhibitors, standalone or in combination with immune checkpoint blockade therapies<sup>2,7,8</sup>.  
56 However, owing to a high degree of intra- and inter-tumor heterogeneity, these treatments  
57 benefit only a fraction of patients, and often result in acquired resistance and further disease  
58 progression<sup>2,9</sup>.

59 Recent advancements in microfluidics and molecular barcoding have enabled high-  
60 throughput transcriptional, epigenomic and even multi-omic tissue profiling at the single cell  
61 resolution, yielding important biological insights. For instance, using single-cell RNA  
62 sequencing (scRNA-Seq) a plethora of single-cell resolution healthy and cancerous tissue  
63 atlases have been constructed, revealing the phenotypic complexity and plasticity of the tumor  
64 microenvironment<sup>10-13</sup>. In the context of ccRCC, single-cell techniques have shed light on the  
65 cell of origin of ccRCC<sup>14,15</sup>, malignancy-related transcriptional programs of the tumor<sup>16</sup> and the  
66 heterogeneous tumor-associated immune cell infiltrate<sup>17-20</sup>. Furthermore, the phenotypical  
67 changes of immune cell populations along advancing disease stage<sup>21</sup> and immunotherapy  
68 treatment<sup>18,22</sup> have been characterized in detail.

69 Upon the widespread adoption of the single cell profiling techniques there was a  
70 noticeable paradigm shift in the field of cancer research – a systemic view of the tumor as a  
71 highly orchestrated ecosystem took over the tumor cell-centric point of view. This shift has  
72 highlighted the crucial role of other players in the TME, including various subpopulations of  
73 stromal and endothelial cells that have been discovered to have an impact on disease  
74 progression, response to therapy and patient survival<sup>23,24</sup>. While considerable efforts have  
75 been made to characterize the ccRCC tumor microenvironment at the single cell level, most  
76 of the previous studies focused on tumor or immune cells, leaving the role of other cell types  
77 within the ccRCC TME poorly understood. In this study, we aimed to address this gap by

78 profiling fresh ccRCC tumor and matched healthy adjacent tissue samples using droplet-  
79 based scRNA-Seq, omitting cell sorting and enrichment steps in order to capture the diverse  
80 phenotypes present in the TME, including the stromal cell populations. As a result, we  
81 captured all major specialized epithelial and endothelial cell populations in healthy adjacent  
82 kidney tissue, including a progenitor-like epithelial cell phenotype resembling the cell of origin  
83 for ccRCC. Furthermore, we described five tumor endothelium subpopulations and discovered  
84 a previously uncharacterized tip-like cell phenotype. Within the TME, we identified well-  
85 described immunosuppressive tumor associated macrophage (TAM) populations and  
86 exhausted infiltrating T cells<sup>21</sup>. Through cell-cell communication analysis, we inferred the  
87 interactions between various cell types within the TME, revealing tumor vasculature and  
88 stromal cell involvement in maintaining an immunosuppressive niche. Expression of genes  
89 involved in these interactions was associated with worse overall survival in the TCGA KIRC  
90 cohort. Overall, our results complement ongoing ccRCC TME characterization efforts by  
91 introducing a novel endothelial phenotype and highlighting the importance as well as potential  
92 therapeutic relevance of stromal and endothelial cells in the TME.

93 **RESULTS**

94

95 *Single cell profiling of healthy and tumor tissues reveals inter-patient variability and epithelial*  
96 *ccRCC progenitor-like population in healthy tissue*

97

98 To dissect the transcriptional landscape of the human ccRCC tumor microenvironment  
99 (TME), we profiled fresh tumor (n=8) and healthy adjacent (n=9) kidney tissue samples using  
100 a droplet-based scRNA-seq platform (Figure 1a). To capture the diverse range of cell types  
101 constituting the TME, our experimental strategy involved rapid isolation of dissociated cells in  
102 microfluidic droplets, without any enrichment or sorting steps (see Methods). Following quality  
103 control, batch correction and doublet removal (see Methods), we obtained a total of 50,236  
104 single cell transcriptomes that were then clustered using a graph-based spectral clustering.  
105 The cell types belonging to each cluster were identified manually based on differentially  
106 expressed top 25 marker genes (adjusted p-value <0.05; cluster vs the rest of cells, Mann-  
107 Whitney U test with Benjamini-Hochberg correction), validated by extensive literature review  
108 (Figure 1b, f and Supplementary file Table 1).

109

110 Healthy-adjacent samples displayed all major epithelial and endothelial cell  
111 populations characteristic of a healthy kidney (Figure 1b)<sup>25-27</sup>. By omitting the cell enrichment  
112 step, we could successfully capture diverse cell types that are known to be highly sensitive to  
113 handling and extended workflow procedures<sup>28</sup>. For example, we captured both, ascending  
114 (*DNASE1L3*) and descending (*AQP1*, *SLC14A1*) parts of the vasa recta, as well as glomerular  
115 endothelium marked by *IGFBP5* and *SOST* expression. The epithelial compartment  
116 encompassed cells from various specialized nephron segments, including rare populations  
117 such as intercalating cells of type A and B (expressing marker genes *ATP6V1G3* and  
118 *SLC26A4*, respectively), as well as podocytes (*NPHS2*, *PODXL*). Interestingly, in contrast to  
119 tumor, all healthy tissue samples comprised a population of epithelial progenitor-like cells,  
120 similar to that described by Young *et al.*<sup>14</sup> (Figure 1e). This population expressed genes  
121 associated with de-differentiated injured kidney epithelium, such as *PROM1* and *ITGB8*<sup>29</sup>, as  
122 well as *CD24* and *SOX4*, which have been implicated in kidney development and mark  
123 proximal tubule and distal nephron response to acute kidney injury<sup>30</sup>. Therefore, the epithelial  
124 progenitor-like cell population in our dataset likely represents a de-differentiated phenotype,  
125 and a potential cell of origin for ccRCC disease.

126

127 The tumor samples encompassed localized and locally advanced pT1a and pT3a  
128 pathologic stages of ccRCC (Figure 1c, Supplementary table S1). These samples exhibited  
129 high immune cell infiltration, including several populations of tumor-associated macrophages

130 and T cells (Figure 1b). The stromal cells separated into myofibroblast (type I, IV and VI  
131 collagens, *FN1*, *TIMP2*, *ACTA2*), vascular smooth muscle cell (*TAGLN*, *ACTA2*, *SNCG*) and  
132 mesangial/vSMC (*BGN*, *PDGFRB*, *TAGLN*) clusters. Tumor endothelium completely  
133 separated from healthy-adjacent endothelial populations (Figure 1b) and included ascending  
134 vasa recta-like cells (*ACKR1*, *DNASE1L3*) as well as heterogeneous vasculature  
135 subpopulations expressing tumor-associated endothelial markers *PLVAP*, *VWF*, *SPARC*,  
136 *INSR*, *ANGPT2*, and others (Supplementary tables S2, S3). Tumor vasculature exhibited  
137 distinct expression patterns as compared to healthy endothelium (Figure 1f, 3b). While four  
138 out of five vasculature subpopulations identified in our data have been described previously<sup>14-</sup>  
139<sup>16</sup>, one tumor vasculature subpopulation (Tumor vasculature 3 comprising 151 cells) appeared  
140 to be novel in the context of ccRCC and featured upregulation of *LY6H*, *PGF*, *LOX*, *CHST1*  
141 and type IV collagen (Figure 1f, 3c), consistent with a tip-cell phenotype<sup>31</sup>.

142

143 The tumor cells in all samples expressed canonical markers *CA9*, *NDUFA4L2*, *VEGFA*  
144 and segregated into three subpopulations, out of which one (Tumor cells 1) was patient-  
145 specific (126 cells in population, Supplementary figure S1a, b). Notably, these cells exhibited  
146 elevated expression of progenitor-like phenotype marker *SLC17A3*, which was not highly  
147 expressed in the healthy-adjacent epithelial progenitor cells (Figure 1e, Supplementary figure  
148 S1b). Furthermore, Tumor cells 1 population was the most distinct from other tumor cells  
149 based on unsupervised hierarchical clustering (Figure 1f, Supplementary figure S1b). These  
150 cells over-expressed genes such as vitamin D binding protein *GC* and *HLA-G*, the latter being  
151 involved in immunosuppressive interactions (Figure 2c), as well as *FABP7*, crucial for lipid  
152 uptake and storage in hypoxic conditions when *de novo* lipid synthesis is repressed<sup>32</sup>.  
153 Additionally, these cells were marked by high expression of pan-cancer marker *MDK*<sup>33</sup>, along  
154 with *IFI27* and *SOD2* (Supplementary figure S1b), both of which play a role in interferon  
155 response<sup>22</sup>. Consistently, Tumor cells 1 was the only tumor cell population not enriched for  
156 hypoxia, but instead enriched for oxidative phosphorylation and adipogenesis (Figure 4a).  
157 Considering the elevated expression of *VCAM1* and *SLC17A3*, it is possible to envision that  
158 this small patient-specific population could represent an intermediate progenitor-tumor cell  
159 phenotype.

160

161 The cellular composition of tumor tissues, as expected, displayed noticeable variability  
162 across the patients as compared to their matched pair of healthy-adjacent tissues (Figure 1d,  
163 Supplementary Table S4). A common theme to all tumor samples was a high number of  
164 immune cells infiltrating the TME, accompanied by almost complete loss of specialized kidney-  
165 specific epithelial and endothelial cell populations (Figure 1c, d and Supplementary figure  
166 S1a). Except for Tumor cells 1, no other cell phenotype was patient-specific; cell population

167 composition analysis by patient ID confirmed adequate representation of cells of different  
168 origin (Supplementary figure S1a). To quantitatively assess tumor sample heterogeneity, we  
169 calculated Shannon entropy for each broad cell category<sup>11</sup>. Low entropy values for a cell  
170 phenotype indicate that it is rarely shared between samples, meaning that the level of  
171 heterogeneity within samples is high. In tumor samples, the heterogeneity was highest for  
172 stromal, endothelial and tumor cells, whereas healthy adjacent tissue samples exhibited  
173 comparatively lower heterogeneity (Supplementary figure S1c, d). Such diverse TME  
174 snapshots among different patients in our and other ccRCC studies<sup>15,34</sup> suggest that patient  
175 stratification may rely on the abundance of specific cellular phenotypes within the TME, rather  
176 than patient-specific phenotypes. This underscores the importance of revisiting strategies for  
177 biomarker selection to aid personalized treatment options in ccRCC.

178

179 *Tumor associated macrophages exhibit phenotypic heterogeneity and immunosuppressive*  
180 *tumor-immune interaction signature is associated with poor survival*

181

182 ccRCC is recognized as highly immune infiltrated tumor with a dynamic  
183 microenvironment. The compositional changes that occur along tumor stage progression<sup>21</sup>  
184 and in response to immunotherapy treatment<sup>22,35</sup> have a profound impact on patient survival.  
185 Therefore, the phenotypic states of immune populations represent potentially druggable  
186 targets for advanced and metastatic ccRCC treatments.

187

188 Within the immune compartment, we identified all major lymphoid and myeloid cell  
189 populations including plasma cells (*IGKC*, *IGHG1*), B cells (*CD79A*, *MS4A1*), mast cells  
190 (*TPSB2*), NK cells (*GZMB*, *NKG7*), classical (*CD14*) and non-classical (*FCGR3A*) monocytes  
191 and two major groups of T cells and macrophages (Figure 1b), in concordance with previous  
192 ccRCC studies<sup>18,19,21</sup>. As expected, the tumor samples were enriched in tumor-associated  
193 macrophages (TAMs) that clustered into four transcriptionally distinct subpopulations  
194 (Figure 2a). The TAM 1 and TAM 2 cells expressed genes hinting towards M1 and M2  
195 polarization, respectively (Figure 2a), thus encompassing a traditional view of TAM dichotomy.  
196 However, TAM 3 and TAM 4 subpopulations did not follow a clear activation pattern, despite  
197 their marker genes seemed to reflect an alternatively activated macrophage phenotype  
198 (Figure 1f, Supplementary file 1). For example, while the expression of certain  
199 immunosuppressive genes, such as *MARCO*, were clearly diminished in TAM 3/4 cells, other  
200 immune-response modulating genes such as *VSIG4*<sup>36</sup> or *VSIR* were highly expressed in TAM  
201 4 population. In addition, among all TAM populations, TAM 4 demonstrated the highest  
202 expression of complement system C1Q genes (Figure 2a), products of which are known to  
203 promote tumor progression in ccRCC by interacting with tumor-produced complement system

204 molecules<sup>37</sup>. Interestingly, some complement components were not only specific to the tumor  
205 cells but also present in the stromal compartment, suggesting potential stromal cell  
206 involvement in tumor progression (Supplementary figure S2a). These findings support the  
207 notion that ccRCC TME is enriched in suppressive macrophages that adapt to the  
208 microenvironment-derived signals influencing disease progression<sup>6,10,21</sup>.

209

210 The lymphoid compartment predominantly consisted of CD8 T cells (*CD8B*, *DUSP4*),  
211 CD4 regulatory T cells (*FOXP3*, *TNFRSF4*), resting/memory T cells (*IL7R*, *CD52*), cytotoxic T  
212 cells (*XCL1*, *KLRB1*) and natural killer cells (*GZMB*, *NKG7*). These subpopulations expressed  
213 multiple exhaustion markers (Figure 2b), with classic immune-checkpoint molecule *PDCD1*  
214 expressed abundantly in CD8 T cell cluster and *CTLA4* enriched in regulatory T cells. The  
215 cytotoxic T cell population shared the exhaustion pattern with NK cells characterized by high  
216 expression of *CD160*, *EOMES*, *CD38* and *CD69*. As expected, resting/memory T cells  
217 displayed the least exhausted phenotype compared to other lymphoid cell populations  
218 (Figure 2b). Given the established exhaustion profile of lymphoid cells and  
219 immunosuppressive phenotype of myeloid cells<sup>18,21,38</sup>, we evaluated the crosstalk of these  
220 immune cell populations and tumor cells.

221

222 Receptor-ligand analysis (see Methods) revealed multiple interactions involved in  
223 chemokine processing, immune suppression and sustained survival of tumor cells (Figure 2c,  
224 Supplementary tables S5, S6). For example, tumor cells were predicted to communicate with  
225 monocytes and TAMs through the immune checkpoint *HLA-G* – *LILRB1/2* axis, which is  
226 involved in promoting the immunosuppressive M2 phenotype and immune escape of the  
227 tumor<sup>39</sup>. Interestingly, both pro-inflammatory (M1) and anti-inflammatory (M2) TAMs received  
228 signals from tumor cells via *SPP1* – *PTGER4* interaction, known to promote macrophage  
229 polarization towards tumor supporting phenotype in hepatocellular carcinoma<sup>40</sup>. Another  
230 important interaction observed in the TME involved T-cell co-stimulatory *CD27* – *CD70* axis,  
231 targeted at CD8 T cells and CD4 regulatory T cells. Recent studies have shown that this cell-  
232 cell interaction is associated with a pro-tumoral effect, primarily driven by chronic stimulation  
233 of T cells leading to exhaustion, enhanced survival of regulatory T cells, and recruitment of  
234 TAMs<sup>41</sup>. Furthermore, the expression of interaction signature (gene set of both receptors and  
235 ligands, Supplementary table S7) was associated with significantly lower overall survival  
236 (Figure 2d, Supplementary table S8) and steadily increased along the progression of the  
237 disease in the TCGA KIRC dataset (Figure 2e). Therefore, our analysis of the ccRCC TME  
238 reveals the extensive network of immune and cancer cell interactions that are involved in  
239 establishing an immune-suppressive TME for sustained tumor survival and growth.

240

241 *Tumor endothelial cells are diverse and play a role in re-shaping the tumor microenvironment,*  
242 *associated with worse overall survival*

243

244 The highly vascularized appearance of ccRCC tumors is often attributed to the  
245 abnormal accumulation of hypoxia-inducible factors<sup>2,3</sup> that create pseudohypoxic conditions  
246 and subsequently increase production of angiogenic factors. To this day, the heterogeneity  
247 and possible regulatory role of the tumor vasculature in ccRCC remains poorly described.  
248 Focusing on ccRCC endothelium in our scRNA-Seq dataset we identified five tumor  
249 vasculature (TV) subpopulations (Figure 3a, c) that were markedly distinct from healthy kidney  
250 endothelium (Figure 3b) and featured upregulation of genes important in vascularization,  
251 angiogenesis and disease progression. For instance, among the multiple overexpressed  
252 genes (Supplementary table S9), the TV cells displayed elevated levels of the fenestration  
253 marker *PLVAP*, which is recognized as a therapeutic target in hepatocellular carcinoma<sup>42</sup>;  
254 *ANGPT2*, which stimulates angiogenesis in autocrine manner and is involved in recruitment  
255 of immunosuppressive TAMs<sup>43</sup>; *IGFBP7*, which is clinically used acute kidney injury urinary  
256 biomarker<sup>44</sup>. Moreover, endothelial migration stimulating insulin receptor (*INSR*) was  
257 overexpressed in tumor endothelium and is known to be associated with poor overall survival  
258 in bladder cancer, which, similarly to ccRCC, is frequently resistant to VEGF pathway targeted  
259 therapy<sup>45</sup>. These findings highlight the abnormal, fenestrated nature of tumor endothelial cells  
260 and might provide future guidance for tumor-specific vasculature identification in ccRCC.

261

262 Within the tumor vasculature we found an ascending vasa recta-like population that  
263 was transcriptionally closer to the healthy endothelium cells than to other tumor vasculature  
264 cells (Figure 3c), as noted in previous work<sup>15</sup>. Intriguingly, our ccRCC atlas also unveiled a  
265 novel, uncharacterized population of tumor vasculature (referred to as TV 3) that appeared as  
266 the most distinct from the rest of TV cells (Figure 3c). This population was marked by high  
267 expression of tip cell markers *LOX*, *PXDN*, *LY6H* and *PGF*<sup>31,46</sup> (Supplementary figure S3,  
268 Supplementary table S10), indicative of an invasive phenotype. Furthermore, TV 3, along with  
269 TV 1 and TV 4, displayed elevated expression of extracellular matrix constituents, including  
270 pro-angiogenic and potentially pro-metastatic collagen type IV and perlecan (*HSPG2*)  
271 (Figure 3c)<sup>47-49</sup>. Meanwhile, TV 2 overexpressed multiple genes implicated in tumor  
272 progression, such as VEGF receptor *FLT1*, *ESM1*, *ANGPT2*, *KCNE3*, coagulation factor VIII  
273 (*F8*) (Figure 3c), which are involved in tumor-associated angiogenesis<sup>49,50</sup>. In addition, TV 2  
274 was marked by high expression of autotaxin (*ENPP2*), a potent stimulator of tumor  
275 development and invasion, which has been associated with acquiring resistance to the  
276 antiangiogenic drug sunitinib in ccRCC<sup>51</sup> (Figure 3c). Interestingly, a fraction of cells from all  
277 tumor vasculature sub-populations expressed *INHBB* and *SCGB3A1* (Supplementary figure

278 S3), which, in concert with perivascular *TNC* (in our dataset expressed by myofibroblasts,  
279 Figure 5b), have recently been demonstrated to orchestrate the pro-metastatic niche in lung  
280 metastasis models in mice<sup>52</sup>. Thus, the tumor vasculature in ccRCC appears to be highly  
281 heterogeneous and expresses a variety of angiogenesis-related and tumor-promoting factors.  
282

283 Subsequently, we investigated the potential interactions between tumor vasculature  
284 and other cell types within the TME. Cell-cell communication analysis using CellPhoneDB<sup>53</sup>  
285 revealed crosstalk between vascular and immune cells involved in angiogenesis, immune  
286 suppression and adhesion (Figure 3d, Supplementary figure S2b). Unexpectedly, our analysis  
287 revealed that tumor vasculature delivers immunosuppressive signals previously thought to be  
288 confined to the tumor cells, such as the interactions between *TIGIT* and *NECTIN2*  
289 (Supplementary figure S2b) or *HLA-F* and *LILRB1/2* (Figure 3d). Also, we observed several  
290 known interactions mediated by myeloid cell produced TNF- $\alpha$  with tumor endothelium i.e *TNF*  
291 – *NOTCH1* (Supplementary figure S2b), which induces *JAG1* expression and enhances  
292 migration and proliferation of endothelial cells upon subsequent VEGF exposure<sup>54</sup>.  
293 Importantly, a higher degree of cell-cell communication between tumor vasculature and  
294 immune cells, as evaluated by higher expression of receptor and ligand pairs, was found to  
295 result in a significantly lower overall survival in TCGA KIRC cohort (Figure 3e).  
296

297 These findings suggest notable tumor vasculature participation in tumor progression  
298 and tumor microenvironment shaping through the expression of angiogenesis-related genes,  
299 tumor-promoting extracellular matrix molecules, and active immunosuppressive  
300 communication with immune cells.  
301

302 *A novel subpopulation of tumor endothelium expresses genes involved in epithelial-  
303 mesenchymal transition associated with worse patient survival*  
304

305 The novel tip cell-like tumor vasculature population (TV 3 in Figure 3a) expressed *LOX*,  
306 *PXDN*, *LY6H* and *PGF*, which are not only denoted as tip cell markers, but have also been  
307 implicated in tumor growth promotion within the TME. For example, placental growth factor  
308 (*PGF*), a member of VEGF family, can directly interact with VEGF receptors and increase  
309 vascular permeability while promoting M2 macrophage polarization<sup>55</sup>. In *PGF*-deficient mice,  
310 tumor-associated M1 macrophage polarization is largely restored while tumor vasculature  
311 appears normalized<sup>56</sup>. Lysil oxidase *LOX* and peroxidase *PXDN* are involved in cross-linking  
312 of the collagen type IV rich extracellular matrix and basement membrane, which is essential  
313 for growth factor induced endothelial cell proliferation and survival<sup>57</sup>. Inhibition of ECM cross-  
314 linking through lysil oxidase knockdown has been shown to impair vessel sprouting<sup>31</sup>.

315 Therefore, the tumor vasculature 3 population represents the leading tip cell phenotype in  
316 angiogenic sprouting and is potentially involved in promoting tumor progression.

317

318 Molecular Signatures Database Hallmark gene set over-representation analysis in  
319 tumor, tumor vasculature and stromal cell populations (top 100 marker genes) revealed, as  
320 expected, hypoxia and glycolysis terms in tumor cells (Figure 4a, Supplementary table S11).  
321 However, this analysis also uncovered an enrichment of epithelial-mesenchymal transition  
322 (EMT) associated genes in all tumor vasculature and stromal cell subpopulations.  
323 Interestingly, the overexpression of EMT pathway overlapping genes for AVR-like tumor  
324 vasculature (Figure 4b) and TV 3 population (Figure 4c) was associated with a significantly  
325 worse overall survival in the TCGA KIRC cohort. In this context, it is important to note that the  
326 specific genes overlapping with the EMT differed between these subpopulations  
327 (Supplementary table S12). Also, even though other cell populations, such as stromal cells  
328 and the rest of tumor vasculature had a significant overlap with the EMT pathway  
329 (Supplementary figure S4a), no effect on patient survival in the TCGA KIRC cohort was  
330 observed (Supplementary figures S4b-g). Overall, our findings highlight the presence of a tip  
331 cell-like tumor endothelium subpopulation associated with an aggressive phenotype,  
332 potentially influencing ccRCC disease progression and survival.

333

334 *Stromal cells remodel the ECM and potentially contribute to immunosuppression of TAM  
335 populations*

336

337 Finally, we investigated the putative roles of stromal cells in the ccRCC tumor  
338 microenvironment. While stromal cells have been recognized as important components of the  
339 TME<sup>34</sup>, their specific contribution in ccRCC have received much less attention compared to  
340 immune or tumor cells. Graph-based clustering of our dataset revealed three cell populations  
341 within the stromal cells: vascular smooth muscle cells (vSMCs), myofibroblasts and  
342 mesangial/vSMCs (Figure 5a, b, Supplementary table S13). The vSMCs expressed markers  
343 *TAGLN*, *ACTA2* and *MYH11*, while myofibroblasts were enriched for ECM constituents  
344 (Collagen types I, III, IV, VI and fibronectin) including markers *TIMP1* and *ACTA2* (Figure 5b).  
345 The precise annotation of the third stromal cell population was challenging due to  
346 simultaneous upregulation of mesangial marker *PDGFRB* and vSMC genes (Supplementary  
347 file Table 1). Interestingly, this population featured substantial transcriptional differences  
348 between tumor and healthy tissue (Supplementary figure S5, Supplementary table S14). In  
349 tumor samples, the mesangial/vSMC population overexpressed tumor marker *NDUFA4L2* as  
350 well as some stress-related genes, such as *CD36*, which is upregulated in chronic kidney  
351 disease and associated with poor prognosis in ccRCC<sup>58,59</sup>, and renin (*REN*), which is

352 expressed by mesangial cells under disturbed homeostasis<sup>60</sup> (Supplementary figure S5).  
353 Thus, it appears that the mesangial/vSMC population is reactive to the disruptive  
354 microenvironmental changes exerted by the tumor.

355

356 Cell-cell interaction analysis between stromal and immune cells revealed putative  
357 interactions related to stromal cell proliferation and survival, as well as immune cell  
358 suppression and adhesion. Majority of immunosuppressive signals originating from the  
359 stromal cells were directed at TAM 1 and TAM 2 subpopulations (Figure 5c). For instance, we  
360 identified *ANXA1* – *FPR1* interaction, which is involved in anti-inflammatory macrophage  
361 polarization and tumor progression in various cancers<sup>61,62</sup>. Furthermore, we found an  
362 indication of myofibroblast and mesangial/vSMC communication with cytotoxic T cells via  
363 *HLA-E* – *KLRC1*, which has recently been proposed as a new targetable path of T cell  
364 exhaustion in bladder cancer<sup>63</sup>. Treatment of *HLA-E* positive tumors with anti-*KLRC1*  
365 antibodies has shown a strong effect in restoring the anti-tumor immunity<sup>64</sup>. Interestingly, our  
366 analysis shows that this communication signature is associated with worse overall survival in  
367 the TCGA KIRC dataset (Figure 5d), and the expression of genes involved in the stromal-  
368 immune cell communication increased with advancing stage of the disease (Figure 5e).  
369 Collectively, our results suggest that stromal cells are actively involved in modulating the tumor  
370 microenvironment in ccRCC through therapeutically relevant paths.

371 **DISCUSSION**

372

373 The single-cell transcriptomic studies have provided valuable insights about the origin  
374 of ccRCC<sup>14,15</sup>, malignancy programs of the tumor<sup>16</sup>, immune cell population phenotypical  
375 changes during tumorigenesis<sup>21</sup> and immunotherapy treatment<sup>18,22</sup> among other.  
376 Complementing these ongoing efforts to better characterize ccRCC tumor microenvironment  
377 we profiled single-cell transcriptomes of human ccRCC tumor samples along with healthy  
378 adjacent tissues. In contrast to previous studies that used cell enrichment prior to scRNA-Seq,  
379 our strategy relied on a rapid isolation of cells from ccRCC specimens, without involving any  
380 type of sorting or cell enrichment. As a result, we could capture a rich diversity of cells  
381 constituting heterogeneous TME that were either significantly depleted or absent in previous  
382 studies. Given that immune compartment in our dataset largely recapitulated previous  
383 findings<sup>17-22</sup>, we mainly focused on the phenotypic heterogeneity and cellular interactions of  
384 the often overlooked and underappreciated endothelial and stromal cell populations.

385

386 Endothelial cells are very important in ccRCC tumorigenesis and to this day remain  
387 the main targets of therapeutics in advanced and metastatic disease<sup>2</sup>. The tumor endothelial  
388 cells identified in our study include a novel, previously uncharacterized tip cell phenotype,  
389 enriched for epithelial-mesenchymal transition pathway genes that are associated with poor  
390 overall survival. Indeed, the previous single-cell studies in ccRCC have also captured  
391 endothelial cells, however, these were most often represented by two major phenotypic  
392 subpopulations that are also found in our ccRCC atlas. For instance, *Zhang et al.*, reported  
393 *ACKR1*+ and *EDNRB*+ endothelium, while *Long et al.* reported *VCAM1*+ and *VCAM1*-  
394 vasculature populations. Consistently, in our dataset we find a population co-expressing  
395 ascending vasa recta marker *ACKR1* and *VCAM1* (tumor AVR-like vasculature), however,  
396 *EDNRB* is expressed by tumor vasculature 1, 2, and 4 populations, but not by tumor  
397 vasculature 3 (Supplementary figure S3), further supporting that this endothelial (*PECAM1*+)  
398 phenotype has not been characterized in ccRCC.

399

400 The tip cell population (TV 3) in our dataset shares similarities with a tip cell population  
401 observed in lung cancer (*LOX*, *PXDN*, *PGF*, *LXN*, collagen type IV enriched) where it was  
402 shown to correlate with worse patient survival<sup>31</sup>. The authors have found this phenotype the  
403 most congruent across several species and tumor types, including kidney cancer (as  
404 determined by bulk proteomics), which raises a question about why previous single-cell  
405 studies of ccRCC did not capture this rare population. Furthermore, the authors demonstrated  
406 that tip cell marker *LOX* knock-down impaired vessel sprouting, suggesting that the reported  
407 population in ccRCC might be of interest for future research as a potential therapeutic target.

408

409 In line with our findings, *Long et al.*, showed that VCAM1+ population (labeled as AVR-  
410 like tumor vasculature in our dataset) is enriched for EMT signature<sup>16</sup>, yet our pathway over-  
411 representation analysis indicates similar association with EMT for all tumor vasculature and  
412 stromal cell populations, not just the AVR-like population (Figure 4a). On another hand, the  
413 worse overall survival in association with EMT was pronounced only for AVR-like and the  
414 tumor vasculature 3 populations, further emphasizing the diversity of tumor endothelial cells  
415 and potential importance of the reported tip cell phenotype. *Alchahin et al.*, also reported  
416 association with EMT for endothelial and stromal cells, but did not discriminate healthy kidney  
417 and tumor endothelial cells. On the contrary to our findings, they report lower endothelial cell  
418 abundance in tumor samples as compared to healthy tissues<sup>20</sup>. Such discrepancies between  
419 different studies can be related to technical aspects, for instance, processing of the samples,  
420 and further underline the importance for accurate phenotypic characterization of the tumor  
421 vasculature cells in ccRCC.

422

423 Our findings suggest two major modes of action of the tumor vasculature cells in the  
424 TME. First, remodeling of the ECM by active deposition of various ECM constituents and  
425 expression of their modifying agents related to EMT (i.e. *LOX*, *PXDN* in tumor vasculature 3)  
426 and second, active engagement in cellular communication in the tumor microenvironment,  
427 mostly involved in immune suppression and angiogenesis maintenance. Interestingly, spatial  
428 transcriptomic profiling of ccRCC by *Li et al.*, showed that collagen producing endothelial cells  
429 localize at the tumor-normal interface enriched in EMT-high tumor cells and *IL1B*+  
430 macrophages<sup>17</sup>. These findings are also corroborated by our results suggesting that tumor  
431 endothelial cells might indeed contribute to EMT in ccRCC and interact with TAMs. The cell-  
432 cell communication analysis uncovered diverse interactions of clinical relevance enriched in  
433 the tumor vasculature and stromal cell communication with immune cells (Figure 3d, 5c). For  
434 instance, in 2021, a phase I-II clinical trial (ID NCT04913337) began for LILRB1 and LILRB2  
435 inhibitor as a monotherapy or in combination with Pembrolizumab (anti PD-1) for advanced or  
436 metastatic solid tumors, including ccRCC. Inhibition of LILRB2 reprograms myeloid cells to a  
437 stimulatory (pro-inflammatory) state, while inhibition of LILRB1 stimulates the reprogramming  
438 of both myeloid and lymphoid cells. Our analysis suggests that *LILRB1/2*+ immune cells  
439 interact not only with tumor cells, but also with endothelial cells. Similarly, endothelial cell-  
440 expressed *NECTIN2* associated with *TIGIT* expressed by regulatory T cells, an interaction  
441 that has gained increased attention over the last few years and is currently exploited in a  
442 multitude of clinical trials<sup>65</sup>. Another intriguing interaction observed between TV 2 and TAM 2  
443 populations was *SCGB3A1* – MARCO. As demonstrated recently, *SCGB3A1*, a secreted  
444 secretoglobin family member produced by endothelial cells, is a crucial component of a pro-

445 metastatic niche and induces stem cell properties in cancer cells, while macrophages are also  
446 required for the niche maintenance<sup>52</sup>. However, *SCGB3A1* – *MARCO* interaction in ccRCC,  
447 to our knowledge, has not been described.

448

449 It is worth emphasizing that stromal cells in our dataset were involved in  
450 communication with immune cells in a suppressive manner, suggesting their participation in  
451 maintaining a pro-tumorigenic niche, especially considering the difference of  
452 mesangial/vSMCs population expression in tumor vs healthy adjacent tissue. Moreover, the  
453 communication signature expression associated with worse overall survival and increased  
454 along the progression of the disease in the TCGA KIRC dataset. On a side note, increase of  
455 stromal cells has recently been shown in recurrent RCC as compared to primary disease,  
456 furthermore, stromal cell-produced Galectin-1 (*LGALS1*) inhibitor significantly reduced tumor  
457 mass and improved anti-PD-1 immunotherapy efficacy in murine models<sup>66</sup>. Another report  
458 showed that co-targeting stromal cells expressing PDGFRs and endothelial cells expressing  
459 VEGFRs delays tumor vascularization and has clinical efficacy in pancreatic neuroendocrine  
460 tumors<sup>43</sup>. Therefore, there is a need for in-depth characterization of ccRCC stromal cells and  
461 further validation of their pro-tumorigenic properties. Understanding the role of stromal cells in  
462 the TME could provide valuable insights for the development of targeted therapies.

463

464 Overall, our study introduces an invasive tumor-associated endothelial tip cell  
465 phenotype and provides new insights into the characterization of the TME in ccRCC. We  
466 propose that tumor endothelial cells favor tumor progression and potentially metastatic  
467 dissemination through the expression of metastasis promoting factors, specific extracellular  
468 matrix components and indirectly via targetable interactions with immune cells in the TME.  
469 Undoubtedly, future functional studies are needed to elucidate the exact roles of the described  
470 diverse tumor endothelial cells and explore their potential as therapeutic targets in ccRCC.

471 **MATERIALS AND METHODS**

472

473 **Sample acquisition**

474

475 Fresh ccRCC tumor (n=8) and healthy-adjacent (n=9) paired kidney tissues were obtained  
476 from the National Cancer Institute (Vilnius, Lithuania) with a bioethics committee approval  
477 No.2019/2-1074-586. No patient had received prior systemic therapy for their cancer. Samples  
478 were collected during an open or laparoscopic, partial or radical nephrectomy surgery, placed  
479 on ice and rapidly (<1 hour) transferred to the laboratory for dissociation. Sample T1 (tumor  
480 from patient P1) was highly necrotic, thus excluded from analysis. Clinical characteristics of  
481 all samples profiled are provided in Supplementary Table S1.

482

483 **Sample processing**

484 Sample preparation was performed according to the scRNA-Seq protocol<sup>67</sup>, yet without FACS-  
485 based enrichment. Briefly, patient derived tumor tissues were dissociated using Tumor  
486 Dissociation Kit (Miltenyi Biotec, cat.no.130-095-929) in an automated instrument  
487 gentleMACS Octo Dissociator with Heaters (Miltenyi Biotec) as per manufacturer's  
488 instructions. Healthy-adjacent tissues were dissociated using Tissue Dissociation Kit I  
489 (Miltenyi Biotec, cat.no. 130-110-201). After dissociation, red blood cells were removed from  
490 the samples using RBC lysis reagent (Miltenyi Biotec, cat.no.130-094-183). After RBC lysis,  
491 cells were washed 3 times in ice-cold 1X DPBS (Gibco, cat.no. 14080-048) at 500g for 5 min.  
492 Cell viability and count was assessed using Trypan Blue dye (Gibco, cat.no. 15250061) on a  
493 hemocytometer. No further enrichment or selection of cells was performed. Cell suspension  
494 was immediately loaded onto inDrops platform<sup>68</sup> for cell barcoding experiment.

495

496 **Single cell barcoding, library preparation and sequencing**

497 Dissociated cells were isolated in 1 nanoliter droplets and their transcriptomes barcoded using  
498 a modified version of inDrops protocol<sup>69</sup>. Specifically, instead of linear cDNA amplification by  
499 *in vitro* transcription we used template switching and PCR amplification. For that purpose, we  
500 isolated the cells at occupancy 0.1 alongside with barcoding beads (Atrandi Biosciences,  
501 cat.no. DG-BHB-C) and reverse transcription/lysis mix, the latter supplemented with a  
502 template switching oligonucleotide, TSO (see Table 2 for composition). We used cell  
503 barcoding chip (Atrandi Biosciences, cat.no. MCN-05) to inject the cells, DNA barcoding  
504 beads, and RT/lysis mix at flow rates of 250, 60, 250  $\mu$ l/hr, respectively. The droplet  
505 stabilization oil (Atrandi Biosciences, cat. no. MON-DSO2) was set at 700  $\mu$ l/hr. The emulsion  
506 was collected off-chip on ice rack and briefly exposed to UV light (5 min at 6.5 J/cm<sup>2</sup> of 350  
507 nm, Atrandi Biosciences, cat.no. MHT-LAS2) to release the photo-cleavable RT primers from

508 the barcoding hydrogel beads. The RT reaction was performed at 42 °C for 60 min followed  
509 by 5 min at 85 °C. The post-RT emulsion was burst with 10% emulsion breaker (Atrandi  
510 Biosciences, cat.no. MON-EB1) and pooled material was used for subsequent library  
511 construction.

512

### 513 **Library construction**

514 The barcoded-cDNA was purified twice with 0.8X AMPure XP reagent (BeckMan Coulter,  
515 cat.co. A63881) as per manufacturer's instructions. Next, cDNA was PCR amplified with KAPA  
516 HiFi Hot Start Ready Mix (Roche, cat.no. KK2601) using cDNA FWD primer and cDNA REV  
517 primers (see Table 3). Amplified DNA was fragmented and ligated to adapter using instruction  
518 and reagents provided by NEBNext® Ultra™ II FS DNA Library Prep (NEB, cat.no. E7805S).  
519 Finally, the libraries were amplified by 12-rounds of indexing PCR (2X KAPA HiFi Hot Start  
520 Ready Mix, Roche, cat.no. KK2601). Library quality was assessed using Bioanalyzer DNA  
521 High Sensitivity chip (Agilent, cat.no. 50674626). The libraries were sequenced on Illumina  
522 NextSeq 550 platform in multiple batches using either NextSeq 500/550 High Output Kit v2.5  
523 (75 Cycles) (Illumina, cat.no. 20024906) or NextSeq 500/550 High Output Kit v2.5 (150  
524 Cycles) (Illumina, cat.no. 20024907).

525

### 526 **Raw sequencing data processing**

527 The STARsolo pipeline (<https://github.com/jsimonas/solo-in-drops>) was used to process the  
528 data and to obtain expression matrices. STAR (version 2.7.6a) was run with the following  
529 parameters: --soloMultiMappers Uniform, -- soloType CB\_UMI\_Simple, -- soloUMIfiltering  
530 MultiGeneUMI, and --soloCBmatchWLtype 1MM. Homo sapiens (human) genome assembly  
531 GRCh38 (hg38) and Ensembl v93 annotations were used as the reference.

532

### 533 **Data analysis: quality control, doublet and RBC removal**

534 Starting with cell x gene matrices, analysis was performed in Python using scanpy toolkit  
535 (Table 4). All notebooks are provided at [https://github.com/zvirblyte/2023\\_ccRCC](https://github.com/zvirblyte/2023_ccRCC). Briefly, the  
536 raw count matrices were uploaded into an AnnData object and filtered by total transcript count  
537 and mitochondrial count fraction. The threshold for mitochondrial counts for all libraries was  
538 20%. The total transcript count threshold was determined by evaluating the total count  
539 distribution and was selected permissive at minimum 400 UMIs per cell (300 UMIs for libraries  
540 T3.1, T9.1, N3.3, N4.3, N2.3). Doublets were removed using Scrublet<sup>70</sup> (v0.2.3) in the same  
541 PCA space used for initial UMAP construction. Scrublet was applied on each emulsion  
542 separately. Briefly, the procedure for doublet removal consisted of 1) Calculating doublet  
543 scores for each cell in each emulsion using Scrublet; 2) high resolution graph-based clustering  
544 using Scanpy's Louvain algorithm implementation (resolution = 60); 3) evaluation of mean

545 doublet score and fraction of predicted doublets per cluster; 4) manual inspection of doublet-  
546 rich clusters in the interactive SPRING application<sup>71</sup>, 5) removal of clusters with high mean  
547 doublet score and doublet fraction and no cluster-specific gene expression. This procedure,  
548 starting from UMAP construction at step 2) was repeated a total of 2 times and 913 cells (<2%  
549 of the total cell population) were removed. Transcriptomes with >1% of total raw counts  
550 originating from hemoglobin genes (HBB, HBA1, HBA2, HBD) were considered as red blood  
551 cells (RBCs) and 47 such transcriptomes were removed from further analysis.

552

### 553 **UMAP construction, clustering and annotation**

554 After filtering and QC steps we retained 50,236 single cells that were used to construct a graph  
555 and UMAP representation (Figure 1B). The procedure consisted of 1) normalization to 10 000  
556 total counts, log-transformation and scaling; 2) selection of highly variable genes; 3) PCA; 4)  
557 batch correction using Harmony<sup>72</sup>; 5) graph construction and 6) UMAP representation. After  
558 normalization, genes with 15 CPTT (counts per ten thousand) in not less than 25 cells were  
559 considered abundant and retained, furthermore, mitochondrial and ribosomal genes were  
560 excluded and top 2000 abundant and highly variable genes, based on Fano factor (as in <sup>68</sup>),  
561 were used for PCA. To remove batch effects due to different batches of barcoding beads the  
562 dataset integration was performed using function `scipy.external.pp.harmony_integrate()`  
563 with the batch variable ‘beads’. Then, adjacency graph was constructed using  
564 `sc.pp.neighbors()` with `n_neighbors=30` and UMAP representation was built using `sc.tl.umap()`  
565 with `min_dist=0.4`. The resulting representation was used for exploration in interactive  
566 SPRING application. Graph-based spectral clustering with varying number of clusters (k) was  
567 performed using `sklearn.cluster.SpectralClustering()` function, the clustering results were  
568 explored in the interactive SPRING environment, and `k=43` was selected for annotation.  
569 Differential gene expression analysis (Mann Whitney U test with Bonferroni-Hochberg  
570 correction) was performed and top 25 marker genes for each cluster (adjusted p-value <0.05)  
571 were used for in-depth literature analysis and manual cell type annotation (Supplementary file  
572 Table 1, Supplementary table S2).

573

### 574 **Sample heterogeneity quantification**

575 To quantify sample heterogeneity, Shannon entropy of samples was calculated for each broad  
576 cell category as described in Chan et al.<sup>11</sup> Briefly, entropy values were calculated for sample  
577 frequency in each cell group (stromal, endothelial, tumor, lymphoid, myeloid, epithelial and  
578 cycling). To account for differences in the number of cells per group, we subsampled 100 cells  
579 from each group 100 times with replacement and calculated the Shannon entropy using  
580 function `scipy.stats.entropy()`. Cells from cluster “Tumor cells 1” were excluded, as they were  
581 sample specific.

582

583 **Receptor-ligand interaction analysis**

584 Log-normalized expression values for all cell types, excluding healthy epithelial cell  
585 populations and cycling cells were used to infer cell-cell interactions using CellphoneDB  
586 v.2.0.0<sup>53</sup> with method “statistical\_analysis” and default parameters. Significant (p-value  
587 <0.05) cell-cell interactions were explored and selected interactions are shown in Figure 2C,  
588 3D, 5C and Supplementary Figure 2B. Cell-cell interaction signatures for subsequent  
589 survival analysis (as in Figure 2D) were constructed by taking both the receptor and ligand  
590 genes in the set (provided in Supplementary table S7). Cell-cell interaction analysis results  
591 are provided in Supplementary tables S5 and S6.

592

593 **Gene set over-representation analysis**

594 Gene set over-representation analysis was employed to evaluate the potential functional  
595 significance of a given gene signature. The analysis utilized gene sets obtained from the  
596 Hallmark Pathways of the MSigDB database v7.5.1<sup>73</sup>. Gene signatures were then submitted  
597 to a hypergeometric test implemented in the enrichGO() function of the clusterProfiler R  
598 package<sup>74</sup> using genes that were detected (nonzero UMI counts) in kidney tissue samples as  
599 a universe (background reference). The pathways having FDR (Benjamini-Hochberg) values  
600 below 0.05 were considered as significantly over-represented.

601

602 **Survival analysis**

603 TCGA KIRC cohort bulk RNA-seq (upper quartile FPKM normalized) and clinical data were  
604 downloaded from the NCI GDC Data Portal<sup>75</sup> using the TCGAbiolinks R package<sup>76</sup>. Cell type  
605 signature scoring of the TCGA bulk RNA-seq samples was performed by calculating an  
606 arithmetic mean of the z-score transformed expression values for all genes in a given  
607 signature. The used gene-wise z-score transformation equalized differences in the gene  
608 expression abundances, so that lowly and highly expressed genes would have the same scale  
609 and, thus equal weight in the score. The association between signature score and overall  
610 survival time was assessed by Kaplan-Meier and multivariate Cox regression analyses. Log-  
611 rank tests and Wald tests, respectively, were used to evaluate statistical significance (at level  
612 of 0.05) of the performed survival analyses. For the Kaplan-Meier analysis, stratified signature  
613 (high - greater or equal than the median signature score; low – lower than the median signature  
614 score) was used, while for the multivariate Cox regression analysis, the continuous signature  
615 score values were used with patient age and sex as covariates. The survival analyses were  
616 conducted using the survival and the survminer R packages.

617

618 **Table 1. Reagents and materials used in the study**

Resource	Source	Identifier/ Cat No.
ccRCC and paired healthy adjacent kidney samples	National Cancer Institute, Vilnius, Lithuania	N/A
Tumor Dissociation Kit	Miltenyi Biotec	130-095-929
Tissue Dissociation Kit I	Miltenyi Biotec	130-110-201
RBC lysis reagent	Miltenyi Biotec	130-094-183
DPBS	Gibco	14080-048
Trypan Blue solution	Gibco	15250061
Maxima H- minus reverse transcriptase	Thermo Scientific	EP0751
dNTP (10 mM each)	Thermo Scientific	R0192
RiboLock RNase inhibitor	Thermo Scientific	EO0382
Igepal CA-630	Sigma Aldrich	18896-50mL
AMPure XP reagent	BeckMan Coulter	A63881
2X KAPA HiFi Hot Start Ready Mix	Roche	KK2601
NEBNext Ultra II FS DNA Library Prep Kit	NEB	E7805S
Bioanalyzer DNA High Sensitivity assay	Agilent	50674626
NextSeq 500/550 HO Kit v2.5 (75 Cycles)	Illumina	20024906
NextSeq 500/550 HO Kit v2.5 (150 Cycles)	Illumina	20024907

619

620 **Table 2. Lysis/RT reaction mix for single-cell mRNA barcoding**

Reagent	Amount, $\mu$ l	Concentration in droplet
Nuclease-free water	21	---
5X RT buffer	60	1X

TSO primer (0.5 mM)	15	25 $\mu$ M
dNTP (10 mM each)	15	0.5 mM
10% (v/v) NP-40 (lysis agent)	9	0.3 %
RiboLock RNase Inhibitor	15	1 U/ul
Maxima H minus RT enzyme	15	10 U/ul
Total volume	150	---

621

622 **Table 3. List of DNA oligonucleotides**

Name	Sequence
<b>Template-switching primer</b>	
TSO	5' -AAGCAGTGGTATCAACGCAGAGTACATrGrGrG
<b>cDNA amplification primers</b>	
cDNA REV primer	5' -AAGCAGTGGTATCAACGCAGAGT
cDNA FWD primer	5' -CTACACGACGCTTCCGATCT
<b>Ligation adapter</b>	
Ligation FWD primer	5' -GATCGGAAGAGCACACGTCTGAACCTCCAGTCAC
Ligation REV primer	5' -GCTCTTCCGATCT
<b>Indexing PCR primers</b>	
Forward PCR index primer	AATGATAACGGCGACCACCGAGATCTACACTCTTCCCTACACGACGCTTCCGATCT
PE2-ind1	CAAGCAGAAGACGGCATACGAGAT <b>CGTGAT</b> GTGACTGGAGTTCAGACGTGT
PE2-ind2	CAAGCAGAAGACGGCATACGAGAT <b>ACATCG</b> GTGACTGGAGTTCAGACGTGT
PE2-ind3	CAAGCAGAAGACGGCATACGAGAT <b>GCCTAA</b> GTGACTGGAGTTCAGACGTGT
PE2-ind4	CAAGCAGAAGACGGCATACGAGAT <b>TGGTCA</b> GTGACTGGAGTTCAGACGTGT
PE2-ind5	CAAGCAGAAGACGGCATACGAGAT <b>CACTGT</b> GTGACTGGAGTTCAGACGTGT

PE2-ind6	CAAGCAGAAGACGGCATACGAGAT <b>ATTGGCGTGACTGGAGTCAGACGTGT</b>
----------	--

623

624 **Table 4. Software and algorithms**

Software	Version	Reference
solo-in-drops	v1.0	<a href="https://github.com/jsimonas/solo-in-drops">https://github.com/jsimonas/solo-in-drops</a>
STAR	2.7.6a	<a href="https://github.com/alexdobin/STAR">https://github.com/alexdobin/STAR</a> , <a href="https://doi.org/10.1101/2021.05.05.442755">https://doi.org/10.1101/2021.05.05.442755</a>
scanpy	v1.8.0	<sup>77</sup> , <a href="https://scanpy.readthedocs.io/en/stable">https://scanpy.readthedocs.io/en/stable</a>
harmonypy	v0.0.5	<sup>72</sup> , <a href="https://github.com/slowkow/harmonypy">https://github.com/slowkow/harmonypy</a>
scrublet	v0.2.3	<sup>70</sup> , <a href="https://github.com/swolock/scrublet">https://github.com/swolock/scrublet</a>
SPRING viewer	N/A	<sup>71</sup> , <a href="https://github.com/AllonKleinLab/SPRING_dev">https://github.com/AllonKleinLab/SPRING_dev</a>
scikit-learn	v1.0.2	<a href="https://scikit-learn.org/stable">https://scikit-learn.org/stable</a>
statsmodels	v0.12.2	<a href="https://www.statsmodels.org/v0.12.2">https://www.statsmodels.org/v0.12.2</a>
scipy	v1.6.2	<sup>78</sup> , <a href="https://scipy.org">https://scipy.org</a>
anndata	v0.7.6	<a href="https://doi.org/10.1101/2021.12.16.473007">https://doi.org/10.1101/2021.12.16.473007</a> , <a href="https://anndata.readthedocs.io/en/latest">https://anndata.readthedocs.io/en/latest</a>
numpy	v1.20.1	<a href="https://numpy.org/doc/1.20/index.html">https://numpy.org/doc/1.20/index.html</a>
pandas	v1.2.4	<a href="https://pandas.pydata.org">https://pandas.pydata.org</a>
louvain	v0.7.1	<a href="https://github.com/vtraag/louvain-igraph">https://github.com/vtraag/louvain-igraph</a>
umap	v0.5.1	<a href="https://umap-learn.readthedocs.io/en/latest">https://umap-learn.readthedocs.io/en/latest</a>
matplotlib	v3.2.2	<a href="https://matplotlib.org/stable/index.html">https://matplotlib.org/stable/index.html</a>
seaborn	v0.11.0	<a href="https://seaborn.pydata.org">https://seaborn.pydata.org</a>
jupyterlab	v2.2.6	<a href="https://jupyter.org">https://jupyter.org</a>
CellPhoneDB	v2.0	<sup>53</sup> , <a href="https://cellphonedb.readthedocs.io/en/latest/index.html">https://cellphonedb.readthedocs.io/en/latest/index.html</a>

R	v4.2.1	<a href="https://www.r-project.org/">https://www.r-project.org/</a>
tidyverse	v1.3.2	<a href="https://www.tidyverse.org/">https://www.tidyverse.org/</a>
biomaRt	v2.52.0	<a href="https://bioconductor.org/packages/biomaRt/">https://bioconductor.org/packages/biomaRt/</a>
clusterProfiler	v4.4.4	<a href="https://bioconductor.org/packages/clusterProfiler/">https://bioconductor.org/packages/clusterProfiler/</a>
TCGAbiolinks	v2.24.3	<a href="https://bioconductor.org/packages/TCGAbiolinks/">https://bioconductor.org/packages/TCGAbiolinks/</a>
survival	v3.3-1	<a href="https://CRAN.R-project.org/package=survival">https://CRAN.R-project.org/package=survival</a>
survminer	v0.4.9	<a href="https://cran.r-project.org/package=survminer">https://cran.r-project.org/package=survminer</a>

625

626 **DATA AND CODE AVAILABILITY**

627

628 Upon publication raw data files will be deposited following editorial guidelines. All Jupyter  
629 notebooks for scRNA-seq analysis are available at [https://github.com/zvirblyte/2023\\_ccRCC](https://github.com/zvirblyte/2023_ccRCC).

630

631

632

633 REFERENCES

634

635 1 Hsieh, J. J. *et al.* Renal cell carcinoma. *Nat Rev Dis Primers* **3**, 17009, doi:10.1038/nrdp.2017.9 (2017).

636 2 Dizman, N., Philip, E. J. & Pal, S. K. Genomic profiling in renal cell carcinoma. *Nat Rev Nephrol* **16**, 435-451, doi:10.1038/s41581-020-0301-x (2020).

637 3 Cancer Genome Atlas Research, N. Comprehensive molecular characterization of clear cell renal cell carcinoma. *Nature* **499**, 43-49, doi:10.1038/nature12222 (2013).

638 4 Sato, Y. *et al.* Integrated molecular analysis of clear-cell renal cell carcinoma. *Nat Genet* **45**, 860-867, doi:10.1038/ng.2699 (2013).

639 5 Senbabaooglu, Y. *et al.* Tumor immune microenvironment characterization in clear cell renal cell carcinoma identifies prognostic and immunotherapeutically relevant messenger RNA signatures. *Genome Biol* **17**, 231, doi:10.1186/s13059-016-1092-z (2016).

640 6 Chevrier, S. *et al.* An Immune Atlas of Clear Cell Renal Cell Carcinoma. *Cell* **169**, 736-749 e718, doi:10.1016/j.cell.2017.04.016 (2017).

641 7 Motzer, R. J. *et al.* Avelumab plus Axitinib versus Sunitinib for Advanced Renal-Cell Carcinoma. *N Engl J Med* **380**, 1103-1115, doi:10.1056/NEJMoa1816047 (2019).

642 8 Rini, B. I. *et al.* Pembrolizumab plus Axitinib versus Sunitinib for Advanced Renal-Cell Carcinoma. *N Engl J Med* **380**, 1116-1127, doi:10.1056/NEJMoa1816714 (2019).

643 9 Braun, D. A. *et al.* Interplay of somatic alterations and immune infiltration modulates response to PD-1 blockade in advanced clear cell renal cell carcinoma. *Nat Med* **26**, 909-918, doi:10.1038/s41591-020-0839-y (2020).

644 10 Azizi, E. *et al.* Single-Cell Map of Diverse Immune Phenotypes in the Breast Tumor Microenvironment. *Cell* **174**, 1293-1308 e1236, doi:10.1016/j.cell.2018.05.060 (2018).

645 11 Chan, J. M. *et al.* Signatures of plasticity, metastasis, and immunosuppression in an atlas of human small cell lung cancer. *Cancer Cell* **39**, 1479-1496 e1418, doi:10.1016/j.ccr.2021.09.008 (2021).

646 12 Zilionis, R. *et al.* Single-Cell Transcriptomics of Human and Mouse Lung Cancers Reveals Conserved Myeloid Populations across Individuals and Species. *Immunity* **50**, 1317-1334 e1310, doi:10.1016/j.immuni.2019.03.009 (2019).

647 13 Massalha, H. *et al.* A single cell atlas of the human liver tumor microenvironment. *Mol Syst Biol* **16**, e9682, doi:10.15252/msb.20209682 (2020).

648 14 Young, M. D. *et al.* Single-cell transcriptomes from human kidneys reveal the cellular identity of renal tumors. *Science* **361**, 594-599, doi:10.1126/science.aat1699 (2018).

649 15 Zhang, Y. *et al.* Single-cell analyses of renal cell cancers reveal insights into tumor microenvironment, cell of origin, and therapy response. *Proc Natl Acad Sci U S A* **118**, doi:10.1073/pnas.2103240118 (2021).

650 16 Long, Z. *et al.* Single-cell multiomics analysis reveals regulatory programs in clear cell renal cell carcinoma. *Cell Discov* **8**, 68, doi:10.1038/s41421-022-00415-0 (2022).

651 17 Li, R. *et al.* Mapping single-cell transcriptomes in the intra-tumoral and associated territories of kidney cancer. *Cancer Cell* **40**, 1583-1599 e1510, doi:10.1016/j.ccr.2022.11.001 (2022).

652 18 Krishna, C. *et al.* Single-cell sequencing links multiregional immune landscapes and tissue-resident T cells in ccRCC to tumor topology and therapy efficacy. *Cancer Cell* **39**, 662-677 e666, doi:10.1016/j.ccr.2021.03.007 (2021).

680 19 Borcherding, N. *et al.* Mapping the immune environment in clear cell renal  
681 carcinoma by single-cell genomics. *Commun Biol* **4**, 122, doi:10.1038/s42003-020-  
682 01625-6 (2021).

683 20 Alchahin, A. M. *et al.* A transcriptional metastatic signature predicts survival in clear  
684 cell renal cell carcinoma. *Nat Commun* **13**, 5747, doi:10.1038/s41467-022-33375-w  
685 (2022).

686 21 Braun, D. A. *et al.* Progressive immune dysfunction with advancing disease stage in  
687 renal cell carcinoma. *Cancer Cell* **39**, 632-648 e638, doi:10.1016/j.ccr.2021.02.013  
688 (2021).

689 22 Bi, K. *et al.* Tumor and immune reprogramming during immunotherapy in advanced  
690 renal cell carcinoma. *Cancer Cell* **39**, 649-661 e645, doi:10.1016/j.ccr.2021.02.015  
691 (2021).

692 23 Chen, Y., McAndrews, K. M. & Kalluri, R. Clinical and therapeutic relevance of cancer-  
693 associated fibroblasts. *Nat Rev Clin Oncol* **18**, 792-804, doi:10.1038/s41571-021-  
694 00546-5 (2021).

695 24 Nagl, L., Horvath, L., Pircher, A. & Wolf, D. Tumor Endothelial Cells (TECs) as Potential  
696 Immune Directors of the Tumor Microenvironment - New Findings and Future  
697 Perspectives. *Front Cell Dev Biol* **8**, 766, doi:10.3389/fcell.2020.00766 (2020).

698 25 Stewart, B. J. *et al.* Spatiotemporal immune zonation of the human kidney. *Science*  
699 **365**, 1461-1466, doi:10.1126/science.aat5031 (2019).

700 26 Lake, B. B. *et al.* A single-nucleus RNA-sequencing pipeline to decipher the molecular  
701 anatomy and pathophysiology of human kidneys. *Nat Commun* **10**, 2832,  
702 doi:10.1038/s41467-019-10861-2 (2019).

703 27 Balzer, M. S., Rohacs, T. & Susztak, K. How Many Cell Types Are in the Kidney and  
704 What Do They Do? *Annu Rev Physiol* **84**, 507-531, doi:10.1146/annurev-physiol-  
705 052521-121841 (2022).

706 28 Denisenko, E. *et al.* Systematic assessment of tissue dissociation and storage biases  
707 in single-cell and single-nucleus RNA-seq workflows. *Genome Biol* **21**, 130,  
708 doi:10.1186/s13059-020-02048-6 (2020).

709 29 Schreibing, F. & Kramann, R. Mapping the human kidney using single-cell genomics.  
710 *Nat Rev Nephrol* **18**, 347-360, doi:10.1038/s41581-022-00553-4 (2022).

711 30 Rudman-Melnick, V. *et al.* Single-Cell Profiling of AKI in a Murine Model Reveals  
712 Novel Transcriptional Signatures, Profibrotic Phenotype, and Epithelial-to-Stromal  
713 Crosstalk. *J Am Soc Nephrol* **31**, 2793-2814, doi:10.1681/ASN.2020010052 (2020).

714 31 Goveia, J. *et al.* An Integrated Gene Expression Landscape Profiling Approach to  
715 Identify Lung Tumor Endothelial Cell Heterogeneity and Angiogenic Candidates.  
716 *Cancer Cell* **37**, 21-36 e13, doi:10.1016/j.ccr.2019.12.001 (2020).

717 32 Bensaad, K. *et al.* Fatty acid uptake and lipid storage induced by HIF-1alpha  
718 contribute to cell growth and survival after hypoxia-reoxygenation. *Cell Rep* **9**, 349-  
719 365, doi:10.1016/j.celrep.2014.08.056 (2014).

720 33 Filippou, P. S., Karagiannis, G. S. & Constantinidou, A. Midkine (MDK) growth factor:  
721 a key player in cancer progression and a promising therapeutic target. *Oncogene* **39**,  
722 2040-2054, doi:10.1038/s41388-019-1124-8 (2020).

723 34 Shi, Y. *et al.* Decoding the multicellular ecosystem of vena caval tumor thrombus in  
724 clear cell renal cell carcinoma by single-cell RNA sequencing. *Genome Biol* **23**, 87,  
725 doi:10.1186/s13059-022-02651-9 (2022).

726 35 Au, L. *et al.* Determinants of anti-PD-1 response and resistance in clear cell renal cell  
727 carcinoma. *Cancer Cell* **39**, 1497-1518 e1411, doi:10.1016/j.ccell.2021.10.001 (2021).

728 36 Vogt, L. *et al.* VSIG4, a B7 family-related protein, is a negative regulator of T cell  
729 activation. *J Clin Invest* **116**, 2817-2826, doi:10.1172/JCI25673 (2006).

730 37 Roumenina, L. T. *et al.* Tumor Cells Hijack Macrophage-Produced Complement C1q  
731 to Promote Tumor Growth. *Cancer Immunol Res* **7**, 1091-1105, doi:10.1158/2326-  
732 6066.CIR-18-0891 (2019).

733 38 Pritykin, Y. *et al.* A unified atlas of CD8 T cell dysfunctional states in cancer and  
734 infection. *Mol Cell* **81**, 2477-2493 e2410, doi:10.1016/j.molcel.2021.03.045 (2021).

735 39 Carosella, E. D., Gregori, S. & Tronik-Le Roux, D. HLA-G/LILRBs: A Cancer  
736 Immunotherapy Challenge. *Trends Cancer* **7**, 389-392,  
737 doi:10.1016/j.trecan.2021.01.004 (2021).

738 40 Liu, L. *et al.* Construction of TME and Identification of crosstalk between malignant  
739 cells and macrophages by SPP1 in hepatocellular carcinoma. *Cancer Immunol  
740 Immunother* **71**, 121-136, doi:10.1007/s00262-021-02967-8 (2022).

741 41 Flieswasser, T. *et al.* The CD70-CD27 axis in oncology: the new kids on the block. *J  
742 Exp Clin Cancer Res* **41**, 12, doi:10.1186/s13046-021-02215-y (2022).

743 42 Wang, Y. H. *et al.* Plasmalemmal Vesicle Associated Protein (PLVAP) as a therapeutic  
744 target for treatment of hepatocellular carcinoma. *BMC Cancer* **14**, 815,  
745 doi:10.1186/1471-2407-14-815 (2014).

746 43 De Palma, M., Biziato, D. & Petrova, T. V. Microenvironmental regulation of tumour  
747 angiogenesis. *Nat Rev Cancer* **17**, 457-474, doi:10.1038/nrc.2017.51 (2017).

748 44 Guzzi, L. M. *et al.* Clinical use of [TIMP-2]\*[IGFBP7] biomarker testing to assess risk of  
749 acute kidney injury in critical care: guidance from an expert panel. *Crit Care* **23**, 225,  
750 doi:10.1186/s13054-019-2504-8 (2019).

751 45 Roudnicki, F. *et al.* High expression of insulin receptor on tumour-associated blood  
752 vessels in invasive bladder cancer predicts poor overall and progression-free survival.  
753 *J Pathol* **242**, 193-205, doi:10.1002/path.4892 (2017).

754 46 Abe, Y. *et al.* A single-cell atlas of non-haematopoietic cells in human lymph nodes  
755 and lymphoma reveals a landscape of stromal remodelling. *Nat Cell Biol* **24**, 565-578,  
756 doi:10.1038/s41556-022-00866-3 (2022).

757 47 Elgundi, Z. *et al.* Cancer Metastasis: The Role of the Extracellular Matrix and the  
758 Heparan Sulfate Proteoglycan Perlecan. *Front Oncol* **9**, 1482,  
759 doi:10.3389/fonc.2019.01482 (2019).

760 48 Lindgren, M. *et al.* Type IV collagen as a potential biomarker of metastatic breast  
761 cancer. *Clin Exp Metastasis* **38**, 175-185, doi:10.1007/s10585-021-10082-2 (2021).

762 49 Dumas, S. J. *et al.* Phenotypic diversity and metabolic specialization of renal  
763 endothelial cells. *Nat Rev Nephrol* **17**, 441-464, doi:10.1038/s41581-021-00411-9  
764 (2021).

765 50 Samuelson Bannow, B. *et al.* Factor VIII: Long-established role in haemophilia A and  
766 emerging evidence beyond haemostasis. *Blood Rev* **35**, 43-50,  
767 doi:10.1016/j.blre.2019.03.002 (2019).

768 51 Su, S. C. *et al.* Autotaxin-lysophosphatidic acid signaling axis mediates tumorigenesis  
769 and development of acquired resistance to sunitinib in renal cell carcinoma. *Clin  
770 Cancer Res* **19**, 6461-6472, doi:10.1158/1078-0432.CCR-13-1284 (2013).

771 52 Hongu, T. *et al.* Perivascular tenascin C triggers sequential activation of macrophages  
772 and endothelial cells to generate a pro-metastatic vascular niche in the lungs. *Nat*  
773 *Cancer* **3**, 486-504, doi:10.1038/s43018-022-00353-6 (2022).

774 53 Efremova, M., Vento-Tormo, M., Teichmann, S. A. & Vento-Tormo, R. CellPhoneDB:  
775 inferring cell-cell communication from combined expression of multi-subunit ligand-  
776 receptor complexes. *Nat Protoc* **15**, 1484-1506, doi:10.1038/s41596-020-0292-x  
777 (2020).

778 54 Sainson, R. C. *et al.* TNF primes endothelial cells for angiogenic sprouting by inducing  
779 a tip cell phenotype. *Blood* **111**, 4997-5007, doi:10.1182/blood-2007-08-108597  
780 (2008).

781 55 Lee, W. S., Yang, H., Chon, H. J. & Kim, C. Combination of anti-angiogenic therapy and  
782 immune checkpoint blockade normalizes vascular-immune crosstalk to potentiate  
783 cancer immunity. *Exp Mol Med* **52**, 1475-1485, doi:10.1038/s12276-020-00500-y  
784 (2020).

785 56 Rolny, C. *et al.* HRG inhibits tumor growth and metastasis by inducing macrophage  
786 polarization and vessel normalization through downregulation of PIGF. *Cancer Cell*  
787 **19**, 31-44, doi:10.1016/j.ccr.2010.11.009 (2011).

788 57 Lee, S. W. *et al.* Peroxidasin is essential for endothelial cell survival and growth  
789 signaling by sulfilimine crosslink-dependent matrix assembly. *FASEB J* **34**, 10228-  
790 10241, doi:10.1096/fj.201902899R (2020).

791 58 Yang, X. *et al.* CD36 in chronic kidney disease: novel insights and therapeutic  
792 opportunities. *Nat Rev Nephrol* **13**, 769-781, doi:10.1038/nrneph.2017.126 (2017).

793 59 Xu, W. H. *et al.* Elevated CD36 expression correlates with increased visceral adipose  
794 tissue and predicts poor prognosis in ccRCC patients. *J Cancer* **10**, 4522-4531,  
795 doi:10.7150/jca.30989 (2019).

796 60 Guessoum, O., de Goes Martini, A., Sequeira-Lopez, M. L. S. & Gomez, R. A.  
797 Deciphering the Identity of Renin Cells in Health and Disease. *Trends Mol Med* **27**,  
798 280-292, doi:10.1016/j.molmed.2020.10.003 (2021).

799 61 Araujo, T. G. *et al.* Annexin A1 as a Regulator of Immune Response in Cancer. *Cells*  
800 **10**, doi:10.3390/cells10092245 (2021).

801 62 Moraes, L. A. *et al.* Annexin-A1 enhances breast cancer growth and migration by  
802 promoting alternative macrophage polarization in the tumour microenvironment. *Sci  
803 Rep* **7**, 17925, doi:10.1038/s41598-017-17622-5 (2017).

804 63 Salomé, B. *et al.* NKG2A and HLA-E define a novel alternative immune checkpoint  
805 axis in bladder cancer. *bioRxiv*, 2022.2003.2004.482960,  
806 doi:10.1101/2022.03.04.482960 (2022).

807 64 Andre, P. *et al.* Anti-NKG2A mAb Is a Checkpoint Inhibitor that Promotes Anti-tumor  
808 Immunity by Unleashing Both T and NK Cells. *Cell* **175**, 1731-1743 e1713,  
809 doi:10.1016/j.cell.2018.10.014 (2018).

810 65 Chauvin, J. M. & Zarour, H. M. TIGIT in cancer immunotherapy. *J Immunother Cancer*  
811 **8**, doi:10.1136/jitc-2020-000957 (2020).

812 66 Peng, Y. L. *et al.* Single-cell transcriptomics reveals a low CD8(+) T cell infiltrating  
813 state mediated by fibroblasts in recurrent renal cell carcinoma. *J Immunother Cancer*  
814 **10**, doi:10.1136/jitc-2021-004206 (2022).

815 67 Quintanal-Villalonga, Á. *et al.* Protocol to dissociate, process, and analyze the human  
816 lung tissue using single-cell RNA-seq. *STAR Protocols* **3**,  
817 doi:10.1016/j.xpro.2022.101776 (2022).

818 68 Klein, A. M. *et al.* Droplet Barcoding for Single-Cell Transcriptomics Applied to  
819 69 Embryonic Stem Cells. *Cell* **161**, 1187-1201, doi:10.1016/j.cell.2015.04.044 (2015).  
820 70 Zilionis, R. *et al.* Single-cell barcoding and sequencing using droplet microfluidics. *Nat  
821 Protoc* **12**, doi:10.1038/nprot.2016.154 (2017).  
822 71 Wolock, S. L., Lopez, R. & Klein, A. M. Scrublet: Computational Identification of Cell  
823 Doublets in Single-Cell Transcriptomic Data. *Cell Syst* **8**, 281-291 e289,  
824 doi:10.1016/j.cels.2018.11.005 (2019).  
825 72 Weinreb, C., Wolock, S. & Klein, A. M. SPRING: a kinetic interface for visualizing high  
826 dimensional single-cell expression data. *Bioinformatics* **34**, 1246-1248,  
827 doi:10.1093/bioinformatics/btx792 (2018).  
828 73 Korsunsky, I. *et al.* Fast, sensitive and accurate integration of single-cell data with  
829 Harmony. *Nat Methods* **16**, 1289-1296, doi:10.1038/s41592-019-0619-0 (2019).  
830 74 Liberzon, A. *et al.* Molecular signatures database (MSigDB) 3.0. *Bioinformatics* **27**,  
831 1739-1740, doi:10.1093/bioinformatics/btr260 (2011).  
832 75 Wu, T. *et al.* clusterProfiler 4.0: A universal enrichment tool for interpreting omics  
833 data. *Innovation (Camb)* **2**, 100141, doi:10.1016/j.xinn.2021.100141 (2021).  
834 76 Grossman, R. L. *et al.* Toward a Shared Vision for Cancer Genomic Data. *N Engl J Med*  
835 **375**, 1109-1112, doi:10.1056/NEJMp1607591 (2016).  
836 77 Colaprico, A. *et al.* TCGAbiolinks: an R/Bioconductor package for integrative analysis  
837 of TCGA data. *Nucleic Acids Res* **44**, e71, doi:10.1093/nar/gkv1507 (2016).  
838 78 Wolf, F. A., Angerer, P. & Theis, F. J. SCANPY: large-scale single-cell gene expression  
839 data analysis. *Genome Biol* **19**, 15, doi:10.1186/s13059-017-1382-0 (2018).  
840 79 Virtanen, P. *et al.* SciPy 1.0: fundamental algorithms for scientific computing in  
841 Python. *Nat Methods* **17**, 261-272, doi:10.1038/s41592-019-0686-2 (2020).  
842

## 843 **ACKNOWLEDGEMENTS**

844 We are especially grateful to the patients at the National Cancer Institute, Vilnius, Lithuania  
845 for participating in this study. This work received funding from European Regional  
846 Development Fund [01.2.2-LMT-K-718-04-0002] under grant agreement with the Research  
847 Council of Lithuania. The work in S.Ja. group was funded by grant no. S-MIP-17-54. S. Ju was  
848 supported by the European Union's Horizon 2020 research and innovation programme under  
849 the Marie Skłodowska-Curie grant agreement no. 101030265. We are grateful to Karolis Goda  
850 for wet-lab assistance, Rapolas Zilionis for valuable discussions and input on data analysis,  
851 and the members of the Oncourology Department at the National Cancer Institute (Lithuania)  
852 for their valuable support and kind assistance.

853

## 854 **AUTHOR CONTRIBUTIONS**

855 J.Z., J.N. single-cell RNA-seq experiments, library preparation and sequencing; J.N., R.K.  
856 biospecimen logistics and processing; M.K., A.U., patient consent, biospecimen curation,  
857 acquisition and logistics; J.Z. data analysis and interpretation, initial manuscript draft; S.Ju.  
858 data management and analysis; J.N., S.Ju., S.Ja., L.M. proofreading; J.Z., L.M. manuscript

859 revision and preparation; S.Ja., and L.M. study design and funding acquisition; L.M.  
860 supervision. All authors have read and approved the final manuscript.

861 **FIGURE CAPTIONS**

862

863 **Figure 1.** Profiling the ccRCC microenvironment. a) Experimental design. b) Global single  
864 cell transcriptional map of ccRCC. c) Clinical information of collected samples and  
865 corresponding UMAPs of cells annotated by disease stage (adjacent healthy, pT1a and  
866 pT3a) and patient ID (P1-P9). Healthy adjacent samples (blue) almost completely separate  
867 from the tumor (light and dark red). d) Sample composition by major cell type. Notably,  
868 healthy adjacent samples are enriched with specialized kidney epithelial and endothelial  
869 cells, while tumor samples are enriched for immune cells. e) Expression of ccRCC cell of  
870 origin markers in epithelial progenitor-like cell population. f) Global heatmap for population  
871 specific markers. Only genes with Benjamini-Hochberg adjusted p-value <0.05 are shown.  
872 Color of the gene name indicates major cell type. AVR – ascending vasa recta, DVR –  
873 descending vasa recta, vSMCs – vascular smooth muscle cells, LOH – loop of Henle, tAL –  
874 thin ascending limb, TAL – thick ascending limb, DCT/CNT – distal convoluted/connecting  
875 tubule, ICs – intercalated cells, OM – outer medullary, TAM – tumor associated  
876 macrophages.

877

878 **Figure 2.** Characterization of immune cell populations found in ccRCC. a) Myeloid cell  
879 compartment consists of CD14+ and CD16+ monocytes and 4 populations of tumor  
880 associated macrophages diverse in expression of polarization markers. b) Lymphoid cells in  
881 ccRCC display heterogeneous exhaustion profile. c) Immunosuppressive interactions of  
882 clinical importance revealed by cell-cell communication analysis between immune and tumor  
883 cells using CellPhoneDB. d) Tumor-immune cell interaction signature expression in TCGA  
884 KIRC cohort is associated with a worse overall survival. e) Tumor-immune cell interaction  
885 signature increases along the progression of the ccRCC disease.

886

887 **Figure 3.** Assessing the heterogeneity of tumor vasculature of ccRCC. a) A close-up of  
888 endothelial cell subpopulations. b) Tumor and healthy vasculature comparison shows  
889 upregulation of angiogenesis related genes in tumor vasculature. c) Differential gene  
890 expression between vasculature subpopulations. Only genes with Benjamini-Hochberg  
891 adjusted p-value <0.05 are shown. d) Tumor endothelium and myeloid cells demonstrate  
892 abundant cell-cell interactions. e) Collective tumor vasculature – immune cell communication  
893 signature expression is associated with a worse overall survival in TCGA KIRC dataset. AVR  
894 – ascending vasa recta, DVR – descending vasa recta, TV – tumor vasculature.

895

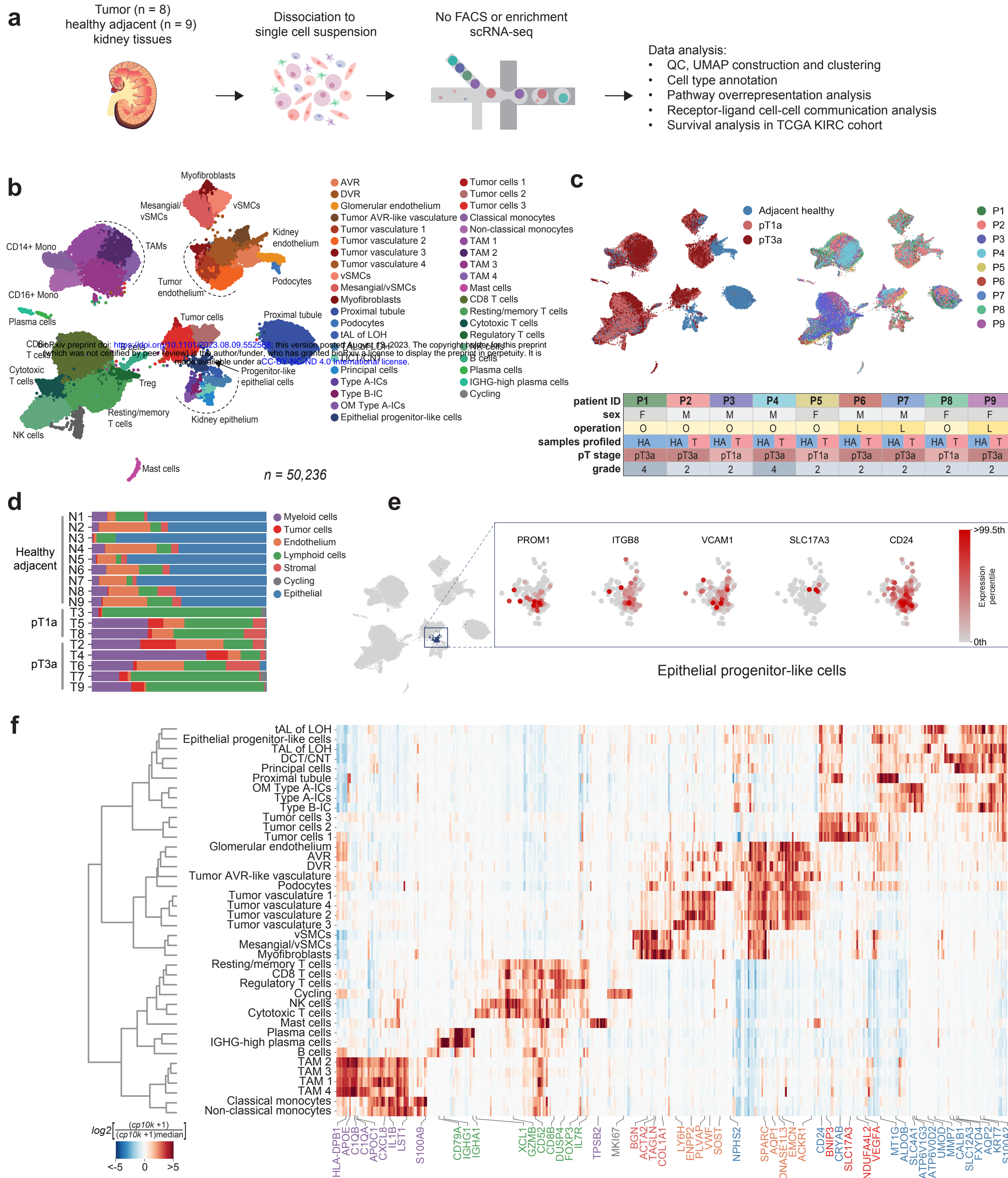
896 **Figure 4.** MSigDB Hallmark pathway overrepresentation analysis. a) Tumor vasculature and  
897 stromal cell populations are enriched in epithelial-mesenchymal transition (EMT) signature.

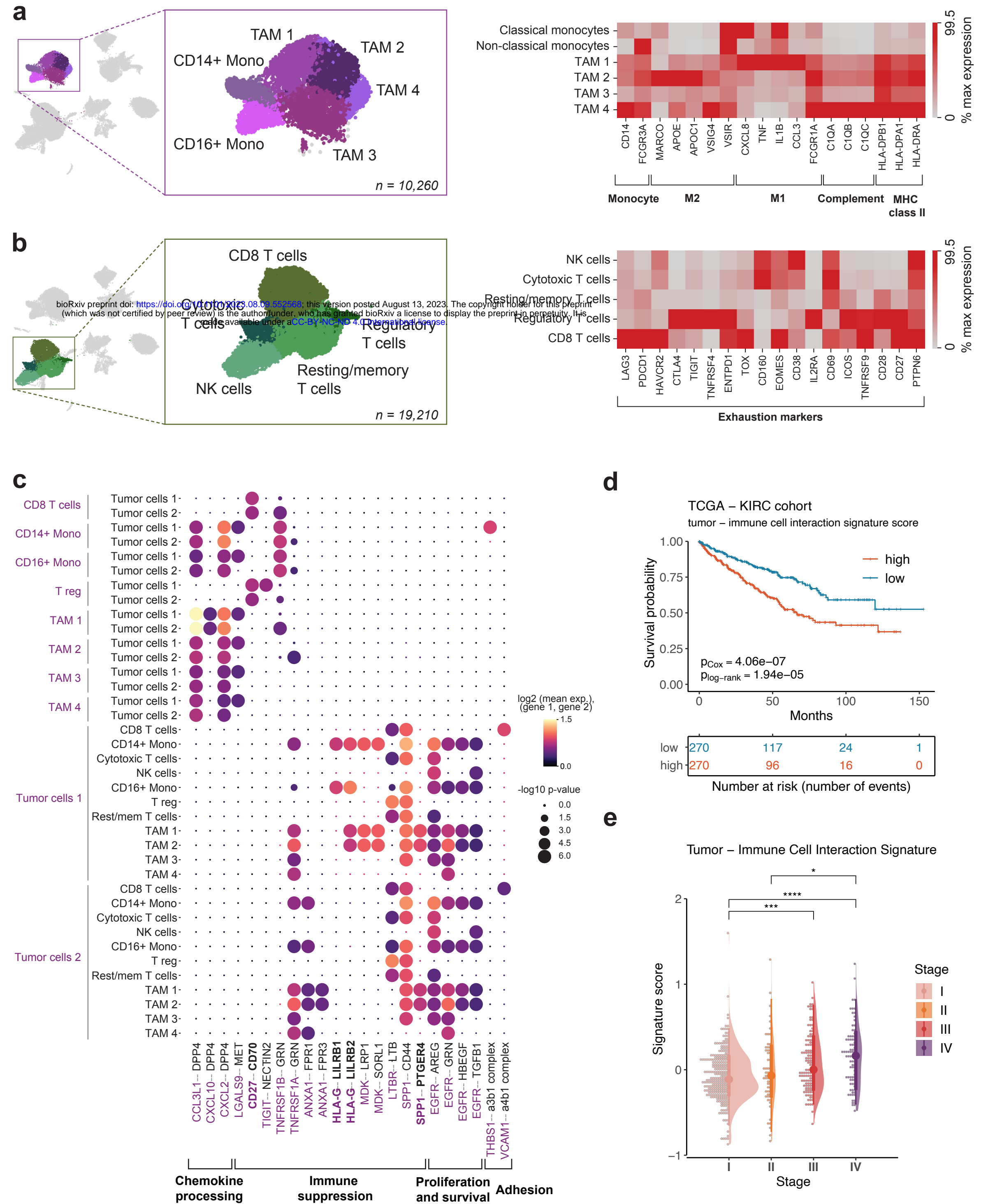
898 b) Tumor AVR-like vasculature and c) tip-like tumor vasculature 3 signature genes  
899 overlapping with EMT pathway associate with worse overall survival in the TCGA KIRC  
900 cohort.

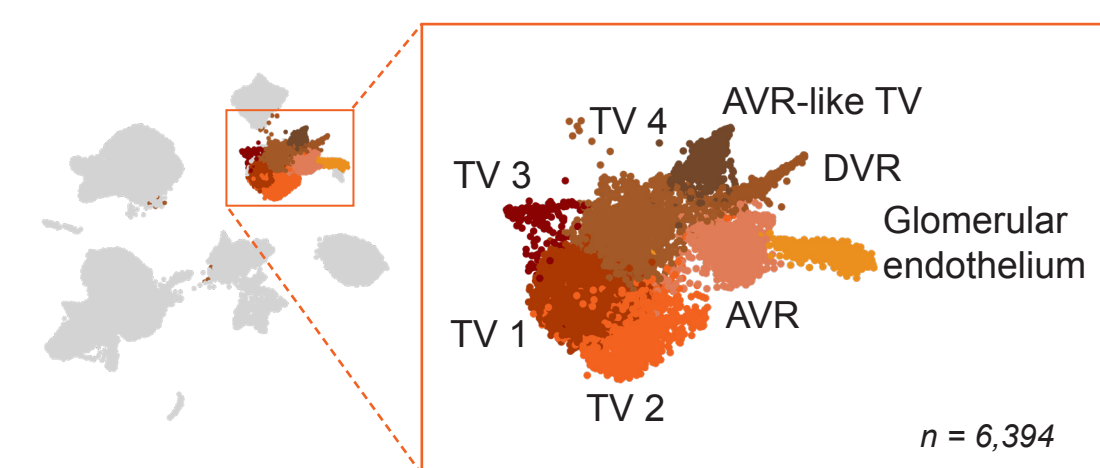
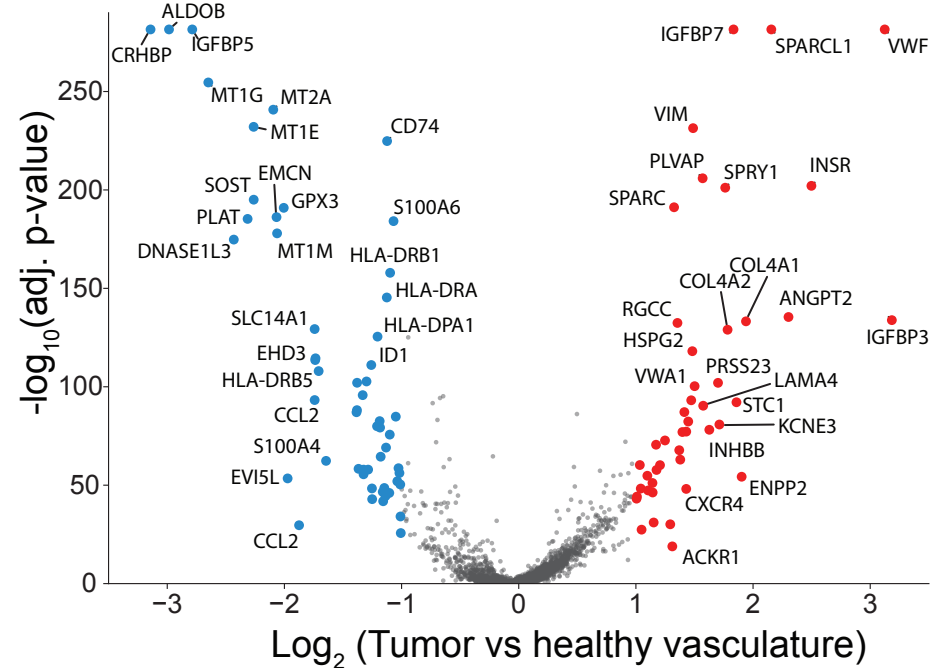
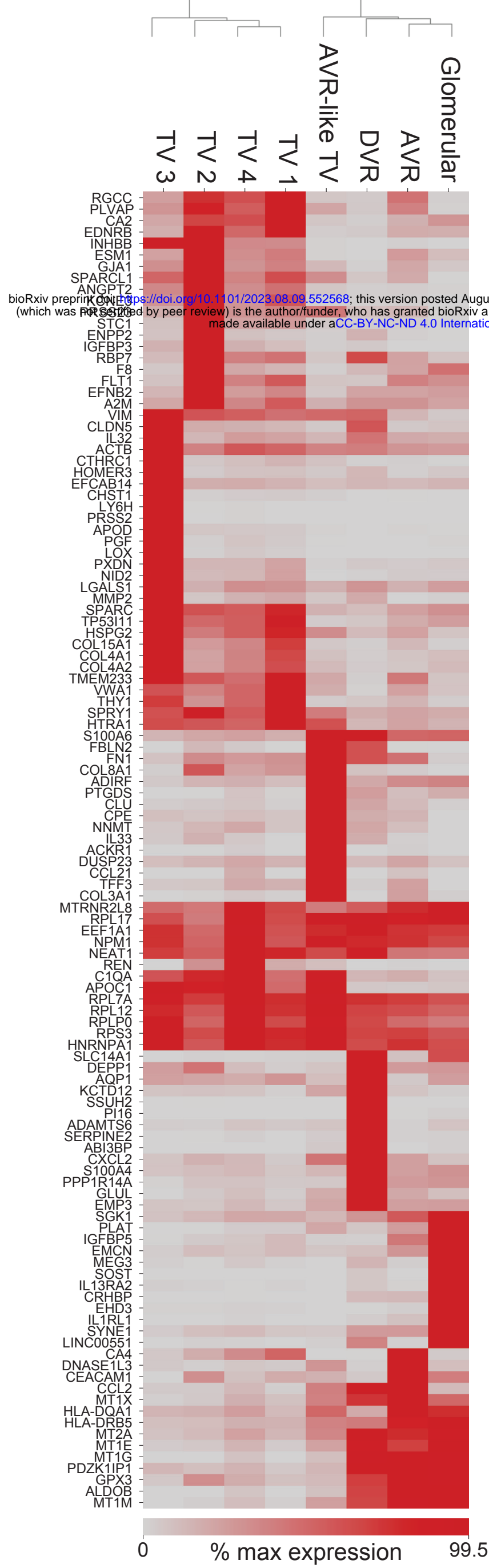
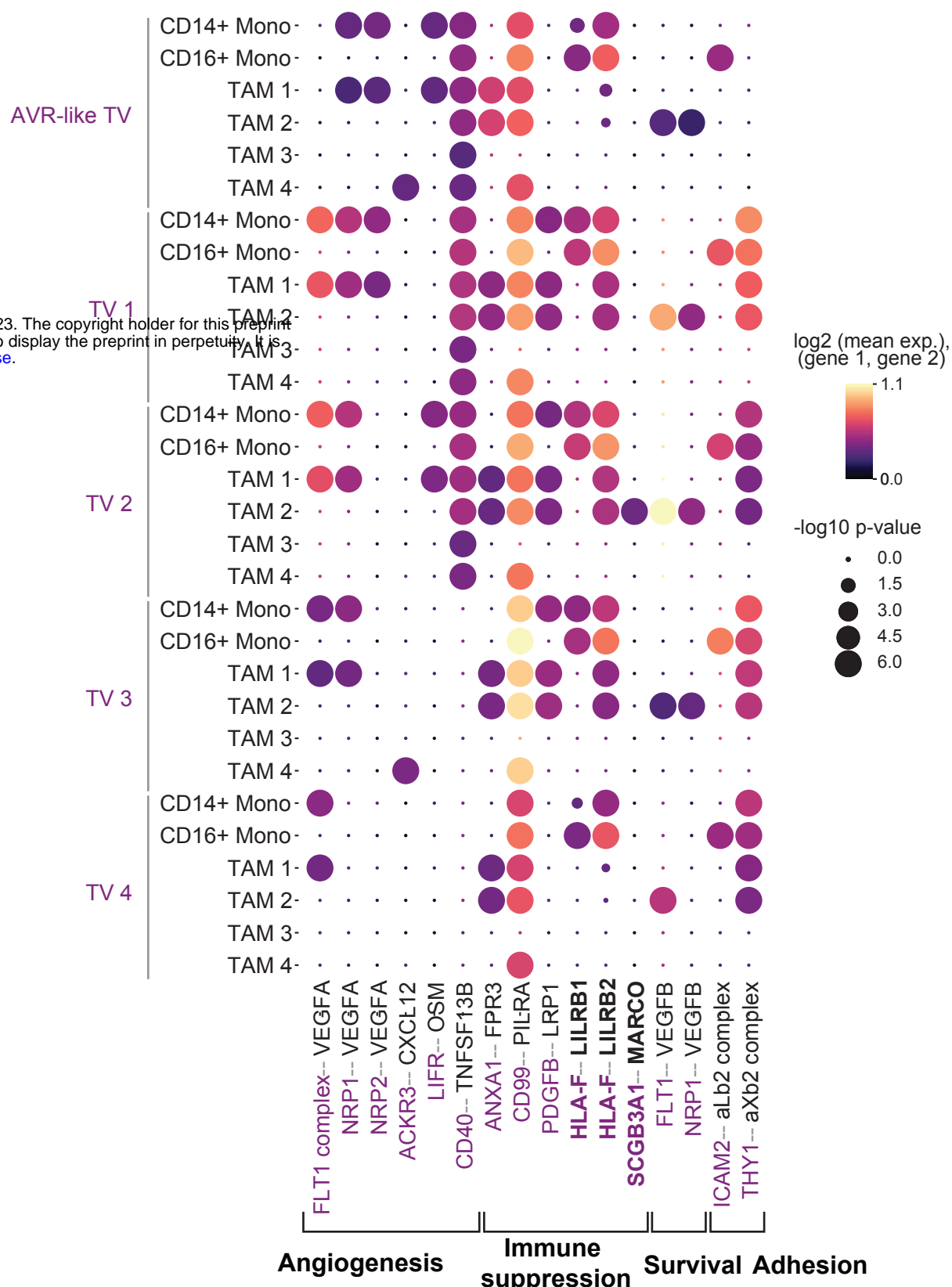
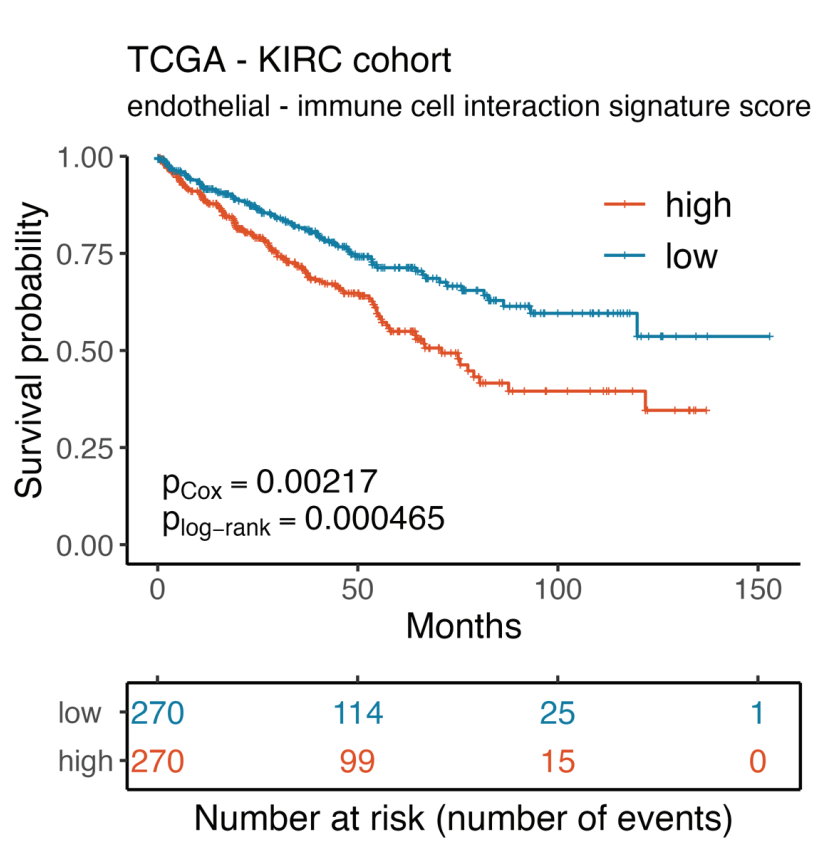
901

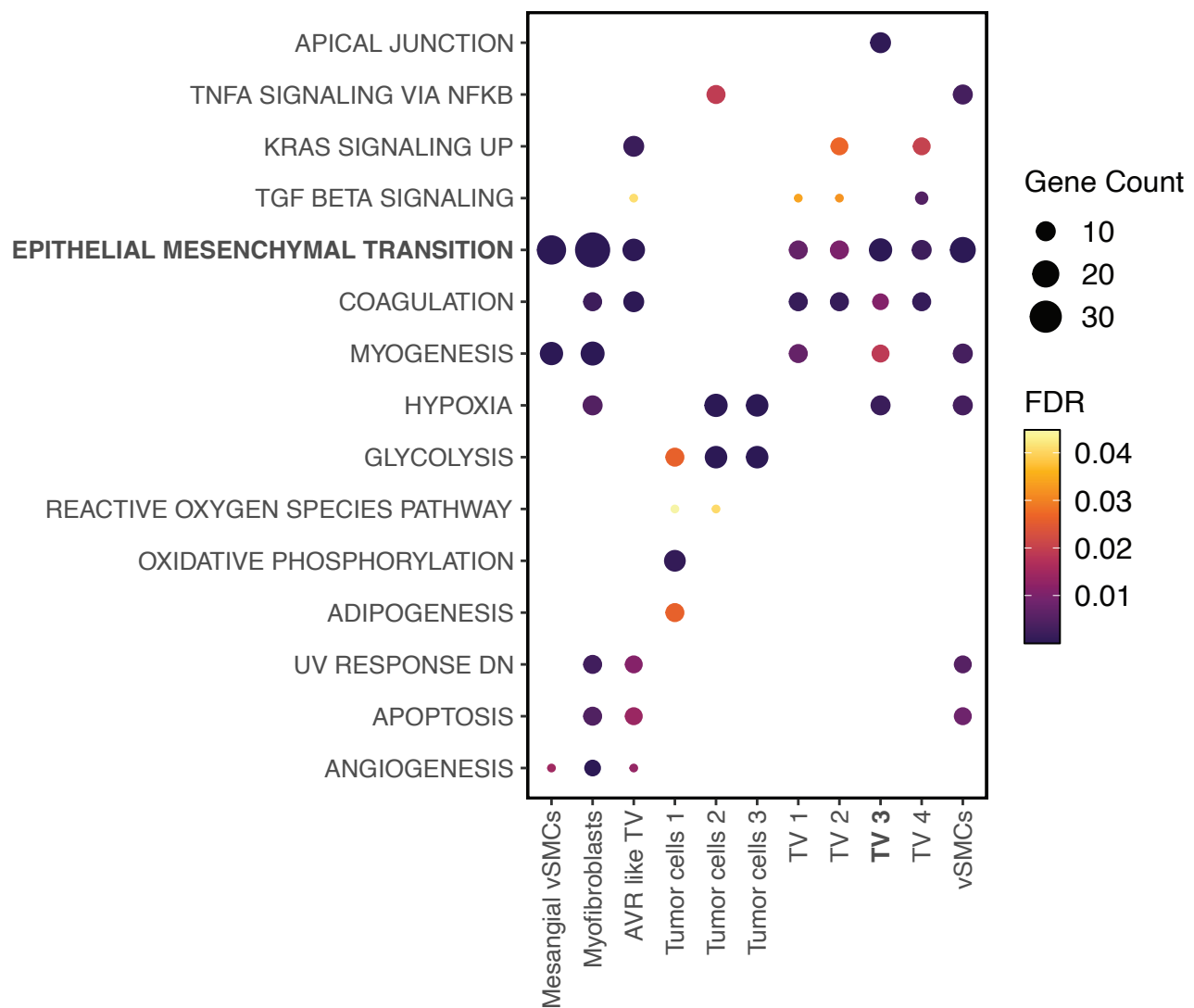
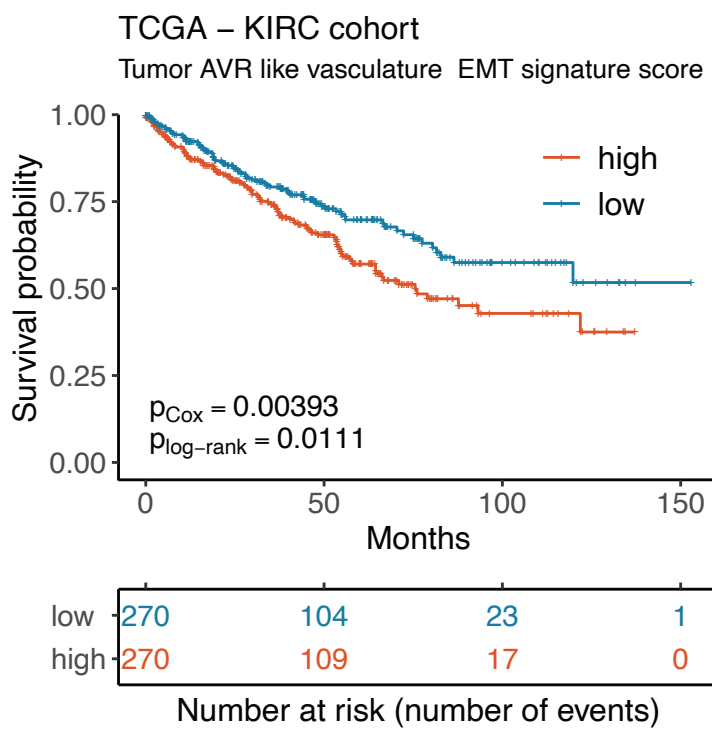
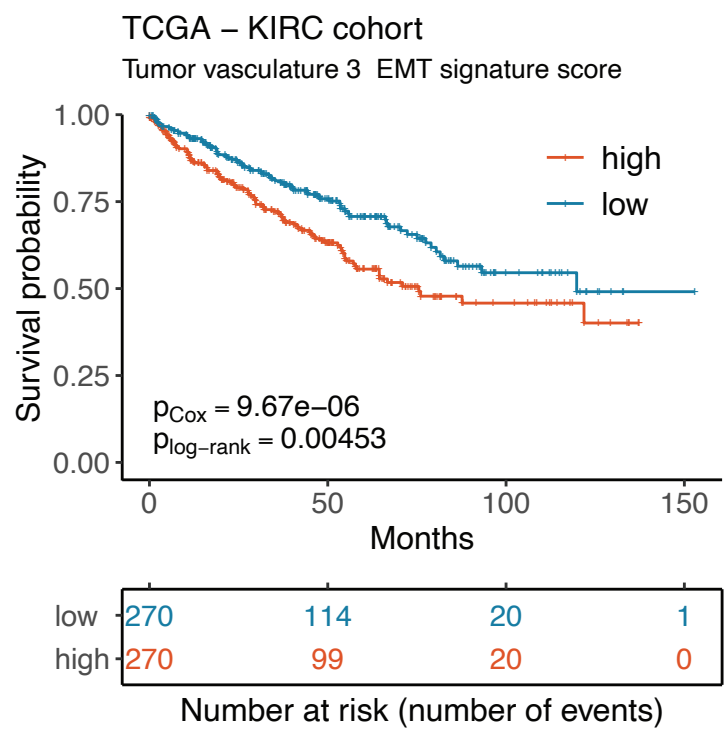
902 **Figure 5.** Assessing the heterogeneity of stromal cells in the TME. a) Stromal cell  
903 populations consisting of vSMCs, myofibroblasts and mesangial/vSMCs. b) Differential gene  
904 expression between stromal cell subpopulations. Only genes with Benjamini-Hochberg  
905 adjusted p-value  $<0.05$  are shown. c) Stromal and immune cells exhibit immunosuppressive  
906 interactions mediated by stromal cells. d) Expression of collective stromal-immune cell  
907 interaction signature gene set associates with worse overall survival in the TCGA KIRC  
908 cohort. e) Stromal-immune cell interaction signature expression increases along the  
909 progression of the ccRCC disease. vSMCs – vascular smooth muscle cells.

910

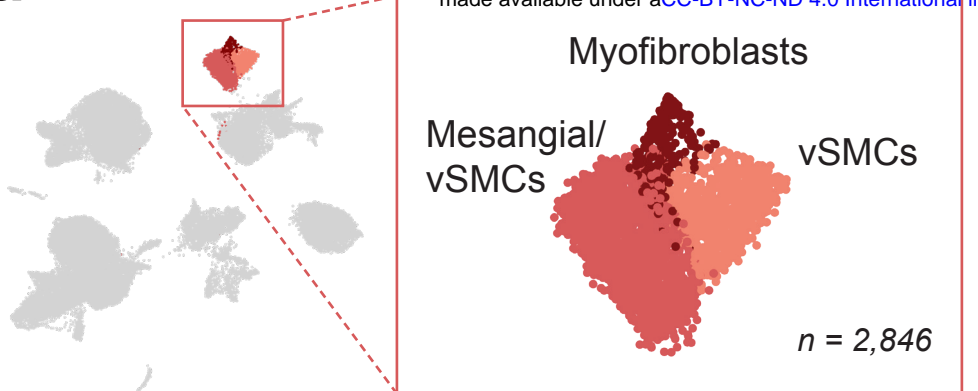




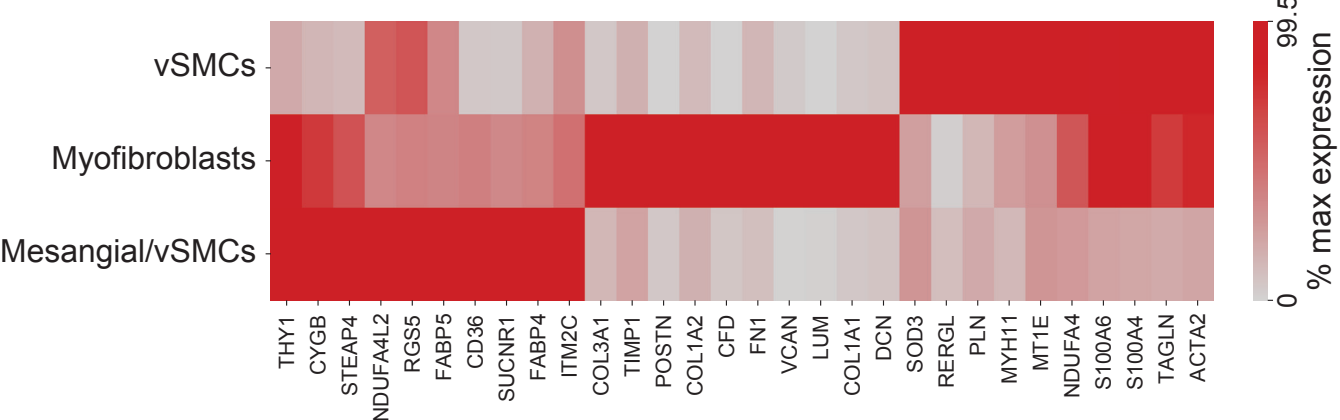
**a****b****c****d****e**

**a****b****c**

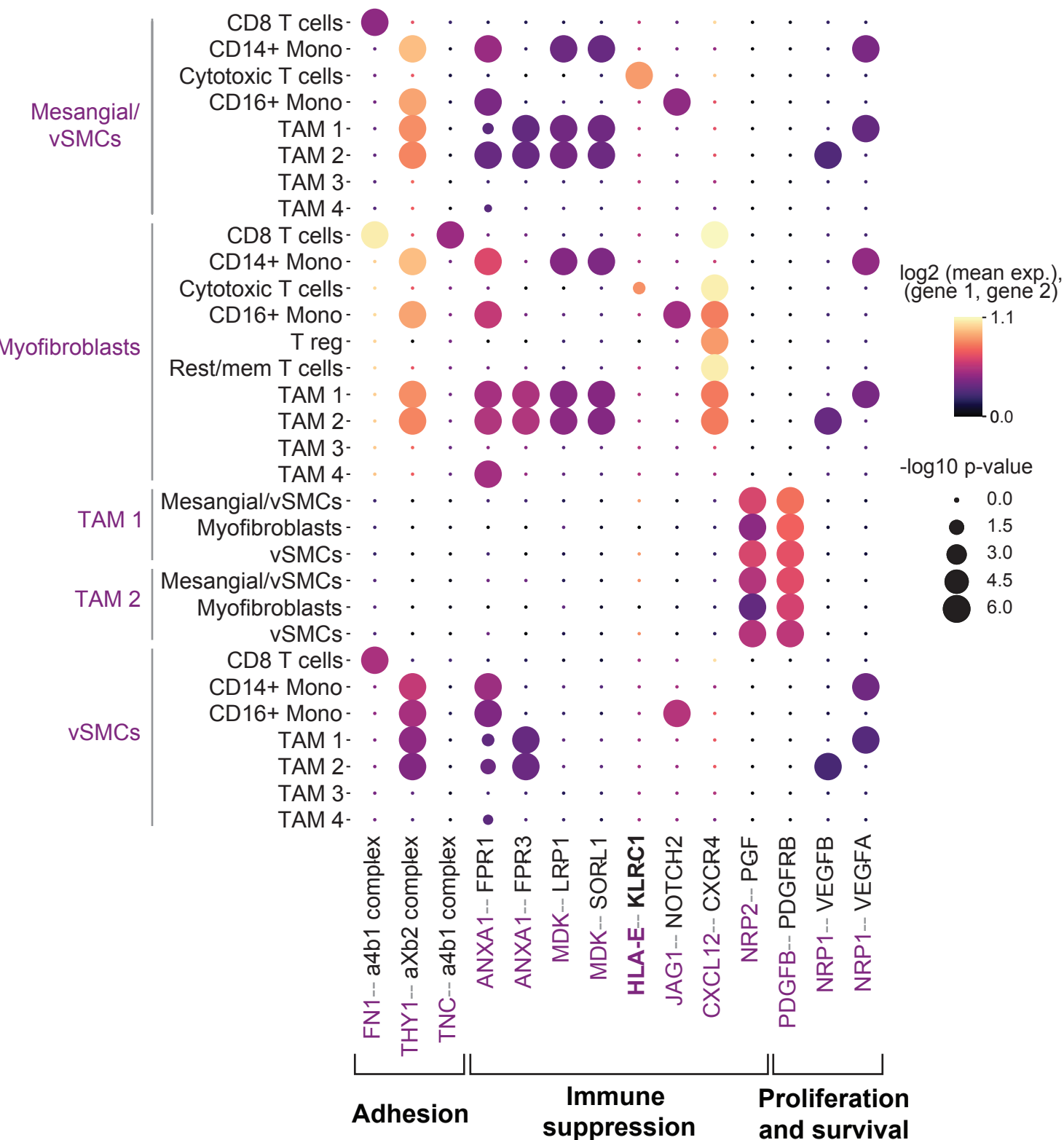
**a**



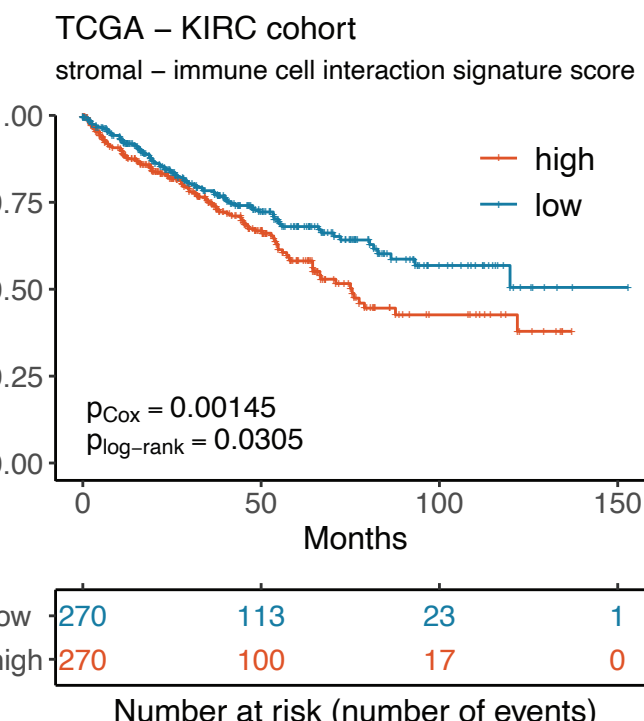
**b**



**c**



**d**



**e**

